UNIVERSITAT JAUME·I

The nature of noise in single-pixel cameras and their application in imaging through scattering media

YESSENIA JAUREGUI SANCHEZ

Doctoral Thesis

Advisors:

Dr. Enrique Tajahuerce

Dr. Jesús Lancis Sáez

Castellón, June 2019

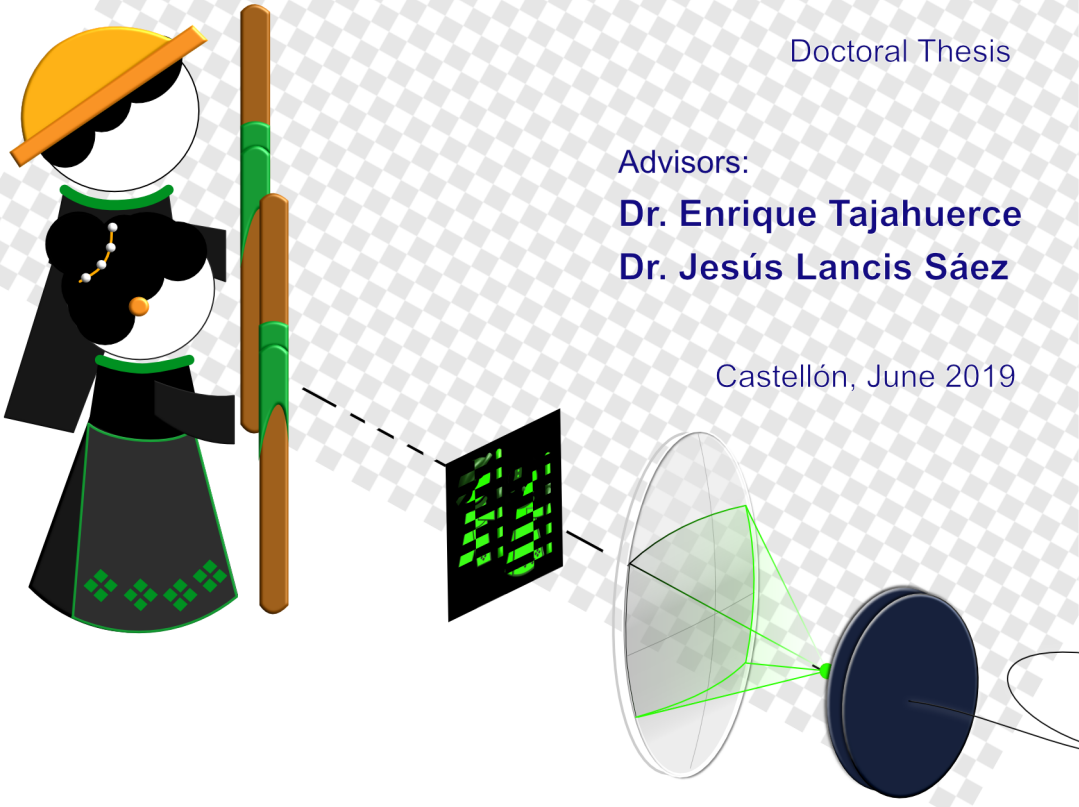

Programa de Doctorat en Ciències

Escola de Doctorat de la Universitat Jaume I

The nature of noise in single-pixel cameras and their application in imaging through scattering media

---

Thesis submitted by

M.Sc. **YESSENIA JAUREGUI SANCHEZ**

in fulfillment of the requirements for

the Ph.D. degree from the Universitat Jaume I

Advisors:

Dr. **Enrique Tajahuerce**

Dr. **Jesús Lancis Sáez**

Castellón de la Plana, June 2019

This doctoral thesis was funded by the following projects:

- Ministerio de Economía y Competitividad (MINECO)
  - FIS2015-72872-EXP
  - FIS2016-75618-R
- Generalitat Valenciana
  - PROMETEO/2016/079
  - GRISOLIA/2015/037
- Universitat Jaume I (UJI)
  - P1-1B2015-35

Meinen lieber Manuel gewidmet

Agradecimientos

Hoy termina una etapa que recordaré con agradecimiento toda mi vida. El corazón me da un vuelco al saber que regresaré a mi amado país México, con la familia que me vio nacer y crecer, con mi familia de sangre. Sin embargo, también llora por aquella que dejaré atrás, por mi familia del corazón, esa que elegí hace cuatro años y que nunca olvidaré.

Podría decir que esta etapa comenzó el 17 de marzo del 2015. Ese día el Dr. Luis Raúl Berriel Valdos, mi tutor en la maestría, me habló de la convocatoria que el Grupo de Investigación en Óptica de Castellón de la Universitat Jaume I (GROC·UJI) había lanzado y que estaba a punto de expirar. Recuerdo que las palabras del Prof. Berriel me perturbaron, pues no sabía si podría dejar a las personas que amaba y continuar sin ellas en otro país, a 12,000 km de distancia. Debo confesar que en ese entonces mi ánimo no era el mejor, tampoco mi estado físico, pero la idea de "empezar de nuevo" en otro país, en otra ciudad, con personas diferentes, me impulsó a participar.

Recordar la mañana del 01 de junio del 2015 aún me llena de emoción. Ese día el Dr. Jesús Lancis me notificó que yo era la *beneficiada seleccionada*

de la beca Santiago Grisolía. Al conocer la noticia, millones de emociones me invadieron, el sentimiento aún sigue siento inefable. Sentí que la vida me daba una oportunidad única y yo decidí agarrarla con fuerza. En ese momento no había espacio para las dudas o el miedo, sólo había arrojo, convicción y agradecimiento para el Dr. Lancis; para el GROC.

Reconozco que los primeros días en España no fueron fáciles, todo parecía nuevo, me sentía sola, confundida y abrumada. Pero el pasar del tiempo, y la buena compañía, hicieron de esta tierra mi casa, mi hogar. Hoy puedo decir que estos años han sido los más felices de mi vida... ¡aquí he aprendido a dar lo mejor de mí, a ser valiente, a volar!

Gracias a los integrantes del GROC: Ángel, Armin, Dani, Eva, Ester, Carlos, Fernando, Gladys, Lluís, Marc, Merche, Miguel, Omel, Pere, Vicente, Dr. Vicent, Dr. Pedro Andrés, Dr. Enrique y Dr. Jesús por su cálida bienvenida. Merche, nunca olvidaré que fuiste la primera persona en recibirme en la estación del tren de Castellón de la Plana; ver una mano amiga después de un largo viaje me reconfortó. Eva, tus palabras siempre fueron un aliciente para mi corazón confundido y solitario. Ester, junto a ti aprendí a reír en *romA*. Ángel, Carlos y Miguel, fueron los mejores compañeros de oficina. Marc, siempre pelearé un hermoso *souvenir* para ti. Armin, te deseo éxito en todo lo que emprendas y como un fotón balístico ¡llega tan lejos como puedas!

Pere, te agradezco infinitamente tu apoyo... ¡no lo habría logrado sin ti!

Por supuesto no olvido a la comunidad internacional del GROC. Thank you so much Mehdi, Razie, Hélène, Ely, Ashi, Taka, Yu, Kohei, Wycliffe Kipnusu, and Prof. Yasuhiro Awatsushi for your support. I will always remember you!

Al Dr. Enrique, mi tutor de tesis, le expreso mi profundo respeto y admiración. Mil gracias por sus enseñanzas y sus consejos... ¡fue un honor aprender este oficio junto a usted!

Por cuatro años la Universitat Jaume I fue mi hogar; aquí conocí personas maravillosas y amigos entrañables. A Pedro y Quino, mis profesores de natación, quiero decirles que junto a ustedes no sólo aprendí a nadar, aprendí a creer en mí... ¡ahora sé que hasta lo inimaginable se puede alcanzar!

Alberto, nunca pensé que en el carril 1 de la piscina de niños encontraría una familia. Te agradezco a ti y a Fátima todas las atenciones que tuvieron conmigo durante mi estancia en España. Muchas gracias por abrirme las puertas de su hogar y adoptarme como un miembro más de ella... ¡siempre los llevaré en mi corazón!

Mariola e Irene, compartir con ustedes el piso fue un placer... ¡rogaré para que algún día nos volvamos a encontrar!

A la comunidad mexicana en España: Laura, Fabiola, Omar, Humberto y Susana, gracias por compartir esta aventura conmigo... ¡a su lado me sentí en nuestra patria!

Finalmente, a mis abuelos, Doña Rosa María Sánchez del Real y Don Alfonso Sánchez Pérez, a mis hermanos, Nitzaye Yutzil, Jaime Alejandro y Ricardo Rodrigo, y a mis amigos en México les agradezco su amor incondicional.

YESSENIA JAUREGUI SANCHEZ

Castellón de la Plana, España, 01 de junio de 2019

Resumen

La adquisición, reconstrucción y procesamiento digital de imágenes es una piedra angular en la comprensión de nuestro entorno. Por ello, en las últimas décadas, sus aplicaciones en distintos campos de la ciencia y la industria han ido en aumento. Sin embargo, a pesar de los avances logrados, las técnicas convencionales de formación de imágenes aún fracasan al intentar adquirir la imagen de un objeto inmerso en un medio turbio como, por ejemplo, una cortina de humo provocado por un incendio, la niebla, el polvo, o los tejidos humanos. Ya que, a diferencia de un medio transparente o semitransparente, las partículas del medio turbio presentan un elevado grado de desorden que provocan el cambio de dirección de los fotones que interactúan con éstas, lo que, junto con el fenómeno de la absorción, hace que la cantidad de información que se puede transmitir a través de éste sea muy baja.

En el 2006 se propuso la cámara de un solo píxel o 'sinlge-pixel camera' como alternativa a la cámara convencional. En ésta, a diferencia de lo que ocurre en una cámara tradicional que utiliza un arreglo matricial constituido por millones de sensores, se usa sólo un sensor. En la cámara 'single-pixel' se proyecta una secuencia de patrones de luz microestructurados sobre el objeto, los cuales son codificados en un modulador espacial de luz program-

able, tipo pantalla de cristal líquido o matriz de microespejos (DMD, de la expresión *digital micromirror device*). La luz reflejada o transmitida por el objeto es colectada con la ayuda de un sistema óptico sencillo y dirigida hacia un detector constituido por un solo píxel, por ejemplo, un fotodiodo. El fotodiodo, previamente sincronizado con el modulador, realiza medidas directas de las proyecciones de la señal-objeto sobre el conjunto de funciones codificadas sobre el DMD. La imagen se obtiene a partir de la resolución de un problema algebraico, bien directamente, o bien utilizando algoritmos de muestreo compresivo tales como los basados en optimización convexa con minimización de la norma L1. En estudios recientes se ha comprobado que la cámara de un solo píxel tiene cierta capacidad para formar imágenes de objetos a pesar de que estos se encuentren inmersos en un medio turbio como el tejido biológico.

Por otra parte, el uso de radiación con longitudes de onda diferentes a las que corresponden al rango visible, en concreto la radiación infrarroja, ha abierto un gran abanico de aplicaciones en el campo de la ciencia y la industria en las últimas décadas. Por ejemplo, en astronomía se usa la radiación infrarroja para estudiar estructuras estelares como galaxias, cúmulos o estrellas inmersas en un disco de materia luminosa y/o polvo. En el campo de la biomedicina, el uso de la imagen infrarroja, aunada a otras técnicas como la tomografía o la mastografía, permite la detección y el diagnóstico no invasivo de enfermedades como el cáncer o el dolor crónico. En la industria, las aplicaciones relacionadas con la adquisición de imágenes con luz infrarroja van desde el diseño de cámaras térmicas, que permiten saber si el aislamiento térmico de un edificio es adecuado o no, hasta la elaboración de complejos sistemas de seguridad. Sin embargo, a pesar de todos los avances realizados, la principal desventaja de la adquisición de imágenes en el infrarrojo es el alto costo de fabricación y mantenimiento de los sistemas ópticos.

En este contexto, el uso de la cámara de un solo píxel en el infrarrojo es una opción que permite reducir los costes de una cámara convencional y al mismo tiempo aprovechar las ventajas antes descritas.

El objetivo general de esta tesis ha sido desarrollar experimentalmente una cámara que permita la adquisición de imágenes a través de diferentes medios turbios en distintas longitudes de onda pertenecientes tanto al rango visible (400–700 nm) como al infrarrojo cercano (800–1000 nm). En este proyecto científico, se han mejorado las prestaciones de la cámara convencional y la cámara de un solo píxel al combinar la iluminación estructurada con la detección por carga de los sensores matriciales (CCD o CMOS). Como resultado, se han obtenido imágenes con mayor calidad y resolución en distintos niveles de iluminación y rangos espectrales. En particular, se han realizado las siguientes actividades: i) la elaboración de un modelo teórico-numérico que nos han permitido evaluar la relación señal-ruido de las imágenes obtenidas con la cámara de un solo píxel en distintas condiciones de iluminación, temperatura y longitudes de onda (del visible al infrarrojo); ii) la construcción y evaluación de una cámara 'single-pixel' con un sensor matricial en el rango visible; iii) la obtención de imágenes a través de medios turbios sintéticos combinando la cámara de un solo píxel con las técnicas de filtraje espacial de Fourier; y iv) el desarrollo de una cámara 'single-pixel' en el rango espectral infrarrojo.

La tecnología propuesta en este proyecto tiene aplicaciones tanto a nivel científico como biomédico e industrial. En el caso de la biomédicina, esta tecnología podría permir alcanzar mayores niveles de penetración y una mejora substancial en la relación señal-ruido de las técnicas de imagen a través de tejidos. Por otro lado, en la industrial, las tecnologías basadas en la cámara de un solo píxel podrían facilitar el desarrollo de protocolos de seguridad con mayor versatilidad, sencillez y menor coste.

Abstract

Imaging through scattering media has been a longstanding issue in many scientific fields. Several optical techniques have emerged to retrieve the information of objects hidden in highly scattering media, for instance, ultrafast time-gating imaging, Fourier spatial filtering, polarization filtering, and wavefront control methods based on measuring the transmission matrix or on adaptive techniques. On the other hand, computational imaging with a single-pixel camera (SPC), or single-pixel imaging (SPI) techniques, have also proved to be a potential approach for imaging through scattering media. Although SPI techniques were proposed in the 1950's, the first efficient SPCs were developed by using a fast programmable spatial light modulator (SLM) in 2006. Since then, SPCs have been successfully applied in many different imaging areas. Among them, we can mention infrared imaging, terahertz imaging, ultrasonic imaging, 3D computational imaging, 3D and photon counting light detection and ranging (LIDAR), stereoscopic imaging, microscopy, holography, and ophthalmoscope imaging.

In the present work, the nature of noise in SPCs has been thoroughly studied and we have addressed the challenge of recovering the image of an object hidden behind scattering media using visible and NIR light. In particular,

we have extensively studied SPI techniques to develop a numerical model of SPC based on photodiodes. This model was characterized by two commercial photodiodes, a Si and an InGaAs biased detector. On the other hand, we have proposed a novel approach for imaging through scattering media that combines the principles of Fourier spatial filtering and SPI techniques. Finally, we have studied experimentally the possibility of performing imaging through turbid media using a SPC setup in a reflection configuration.

Contents

Chapter 1

Introduction

1.1 Motivation and objective

The study of light dates back to ancient times. Following their daily observations, the ancient philosophers asked themselves several questions about the nature of light, its properties, and its interaction with matter. One of the questions that most interested great scientific minds, including Ibn al-Haytham (965–1040 a.C.), Issac Newton (1642–1727 a.C.), Katharine Burr Blodgett (1898–1979 a.C.), among others, was light scattering [1].

The phenomena of light scattering have been studied and described extensively for a long time. Now we know that when light interacts with matter, elastic scattering is present, and any spatial variation in the refractive index contributes to it. By definition, scattering is a process of photon absorption and re-emission without loss of energy but associated with a possibly change in photon direction [2]. We could say that one of the clearest examples of the

process of light scattering, which is caused by scattering of sunlight in the atmosphere, is the blue appearance of clear sky or its reddish appearance at sunrise or sunset. Moreover, this is also the process that gives clouds and milk their white color.

On the other hand, imaging through scattering media has been traditionally challenging in many scientific fields. Several optical techniques have emerged to retrieve the information of objects hidden in highly scattering media, for instance, ultrafast time-gating imaging [3], polarization filtering [4–6], and wavefront control methods based on measuring the transmission matrix [7] or on adaptive techniques [8], and Fourier spatial filtering [9]. This last approach has recently shown promising results in imaging through scattering media in combination with structured illumination [10]. Moreover, single-pixel imaging (SPI) techniques have also proved to be a potential approach for imaging through scattering media [11, 12].

The use of radiation in spectral regions, different to those that correspond to the visible range, in particular, infrared radiation, has also opened a wide range of applications in imaging through scattering media during the last decades. Scattering occurs in all regions of the electromagnetic spectrum, but it is particularly strong in the ultraviolet (<450 nm), visible (450–650 nm), and near-infrared (650–1000 nm) spectral regions [2, 13]. However, in general, light scattering decreases as the wavelength of the light increases.

After a thoroughly study of noise in single-pixel cameras, this thesis addresses the challenge of recovering the image of an object hidden behind a scattering medium. To achieve this goal, we use SPI techniques in two different spectral regions, the visible region, and the near-infrared one, respectively. The general structure of this thesis is outlined below.

1.2 Thesis outline

The thesis is divided into five chapters, including the introduction one. In particular, each chapter covers the following subjects:

In chapter 2, a model of single-pixel cameras (SPCs) based on photodiodes is developed to describe the dependency of the signal-to-noise ratio (SNR) with different optical parameters. Firstly, a theoretical description of SPCs is made. Second, a numerical model of the SPC based on the characteristics of the incident light as well as the specifications of the detector is shown. The model takes into account the photocurrent, the dark current, the photocurrent shot noise, the dark-current shot noise, and the Jonhson-Nyquist (thermal) noise sources and infers the SNR of the SPCs in different contexts. In particular, the SNR as a function of the optical power of the incident light, the wavelength, and the photodiode temperature is analyzed. The results of the model are compared with those obtained experimentally with a SPC.

In chapter 3, a novel approach for imaging through scattering media that combines the principles of Fourier spatial filtering and the SPI technique is shown. First, an experimental arrangement of the SPC working by transmission is carried out to analyze the influence of Fourier spatial filtering on SPI techniques based on photodiodes. As an alternative, a digital camera is used as single-pixel detector to develop a versatile digital Fourier filtering technique. Finally, the technique is used to recover the image of an object hidden behind a scattering medium.

In chapter 4, several experiments for imaging through scattering media using infrared SPCs working by reflexion are described. Firstly, a description

of the experimental configuration of the SPC using IR radiation is made. Second, a study of the quality of the images based on the properties of the scattering media at a wavelength of 650 nm is shown. A comparison of the performance of the SPC at the visible spectral region (650 nm) and NIR (800 nm) is also shown.

Finally, in the last chapter, the main contributions of this research work are emphasized.

1.3 Publications

This doctoral thesis is composed of the following publications:

- **Articles and proceedings**
  - Y. Jauregui-Sánchez, F. Soldevila, P. Clemente, E. Tajahuerce, and J. Lancis, "Imaging through scattering media by Fourier filtering with a single-pixel camera," Proc. SPIE-OSA 10416, Coherence Imaging Techniques and Imaging in Scattering Media II, 10416 (2017). https://doi.org/10.1117/12.2285979
  - Y. Jauregui-Sánchez, P. Clemente, J. Lancis, and E. Tajahuerce, "Imaging through scattering media by Fourier filtering and single-pixel detection," Proc. SPIE 10502, Adaptive Optics and Wavefront Control for Biological Systems IV, 105020W (2018). https://doi.org/10.1117/12.2290274
  - Y. Jauregui-Sánchez, P. Clemente, P. Latorre-Carmona, E. Tajahuerce, and J. Lancis, "Signal-to-noise ratio of single-pixel cameras based on photodiodes," Appl. Opt. **57**, B67–B73 (2018).

https://doi.org/10.1364/AO.57.000B67

– Y. Jauregui-Sánchez, Armin J. M. Lenz, P. Clemente, J. Lancis, and E. Tajahuerce, "Vision through turbid media by Fourier filtering and single-pixel detection," Proc. SPIE 10677, Unconventional Optical Imaging, 1067715 (2018). https://doi.org/10.1117/12.2307366

– Y. Jauregui-Sánchez, P. Clemente, J. Lancis, and E. Tajahuerce, "Single-pixel imaging with Fourier filtering: application to vision through scattering media," Opt. Lett. **44**, 679–682 (2019). https://doi.org/10.1364/OL.44.000679

- **Book Chapter**

  – Y. Jauregui-Sánchez, P. Clemente, P. Latorre-Carmona, J. Lancis, and E. Tajahuerce (2018). Single-Pixel Imaging using Photodiodes [Online First], IntechOpen, DOI: 10.5772/intechopen.79734. Available from: https://www.intechopen.com/online-first/single-pixel-imaging-using-photodiodes

Chapter 2

Single-pixel imaging

Computational imaging with a SPC, or SPI, is a remarkable alternative to conventional imaging [14]. SPCs are based on sampling an object (or a scene) with a sequence of microstructured light patterns codified onto a programmable spatial light modulator (SLM), while the intensity of the light transmitted or reflected by the object is measured by a bucket detector. The image is obtained computationally from the fluctuations of the electrical signal provided by the detector. Thus, the quality of this temporal signal is a key factor in order to recover a high quality image. This technique is closely related to ghost imaging [15–18] and dual photography [19].

The simplicity of the detection procedure in SPI is one of the main advantages of the technique. It can be exploited to use very sensitive light sensors in low light level applications [20, 21]. It is also useful in order to measure the spatial distribution of different parameters such as the spectral content [20, 22] or the polarization state [23] of the light coming from the objects. Besides, SPI has shown robustness to the presence of scattering

media [24, 25]. Moreover, the SPC can be an interesting choice for imaging using light with a spectrum beyond the visible region, such as in the infrared (IR) and terahertz spectral regions.

Among the different possible detectors, photodiodes are the most common sensors in general SPI applications. In this context, we develop a numerical model of a SPC based on a photodiode, which considers the characteristics of the incident light as well as the photodiode specifications. Our model takes into account the photocurrent, the dark current, the photocurrent shot noise, the dark-current shot noise, and the Johnson-Nyquist (thermal) noise. This model allow us to study the signal-to-noise ratio (SNR) as a function of the optical power level and the wavelength of the incident light as well as the photodiode temperature. We restrict our study to silicon (Si) and indium-gallium-arsenide (InGaAs) photodiodes.

In the following sections, firstly, SPCs are described in detail. Second, the properties of the electrical signal provided by photodiodes based on Si and InGaAs materials are reviewed. Third, the numerical model of the SPC is shown. Next, this model is applied to study the SNR of SPCs in different contexts. Some of these numerical results are compared with those experimentally obtained in the laboratory. Finally, the main conclusions are emphasized.

2.1 The single-pixel camera

The ideas on which SPCs are based were already proposed by Golay in 1949 [26] and by Decker in 1970 [27]. However, the first efficient SPC was created in 2006 by using a fast SLM [28]. Since then, SPCs have been

successfully applied in many different imaging areas during the last decade. Among them, we can mention infrared imaging [29, 30], terahertz imaging [31], ultrasonic imaging [32], 3D computational imaging [33, 34], imaging through scattering media [35, 36], 3D and photon counting light detection and ranging (LIDAR) imaging systems [21,37,38], stereoscopic imaging [39], microscopy [40, 41], holography [42, 43], and ophthalmoscope imaging [44].

The architecture of SPCs is basically an optical computer that sequentially computes linear measurements of a selected object or a scene by using light sampling patterns [14]. A schematic representation of the SPC is shown in Figure 2.1. A set of k microstructured light patterns with an irradiance distribution $\psi_k(n, m)$ is codified onto a SLM and sequentially projected onto an object $O(n, m, t)$ at time (t). The light transmitted [see Figure 2.1(a)] or reflected [see Figure 2.1(b)] by the object is collected by a lens and focused onto a photosensor, for instance, a photodiode. The photosensor provides us with an electrical current proportional to the integrated light intensity, which is digitized by a data acquisition system (DAQ). The light intensity (I_{sp}^k) can be represented by the dot product between each microstructured light pattern and the object, i.e.,

$$I_{sp}^k = \sum_{m=1}^{M} \sum_{n=1}^{N} \psi_k(n, m) \cdot O(n, m, t) + \varepsilon(t), \tag{2.1}$$

where $k = 1, \ldots, N \times M$ denotes de pattern index, (n, m) are the discrete spatial coordinates, (N, M) are the two spatial dimensions, and parameter $\varepsilon(t)$ takes into account the measurement noise. In absence of noise, an exact replica of the sampled object is recovered. In this thesis, the object is considered static, therefore $O(n, m, t) = O(n, m)$.

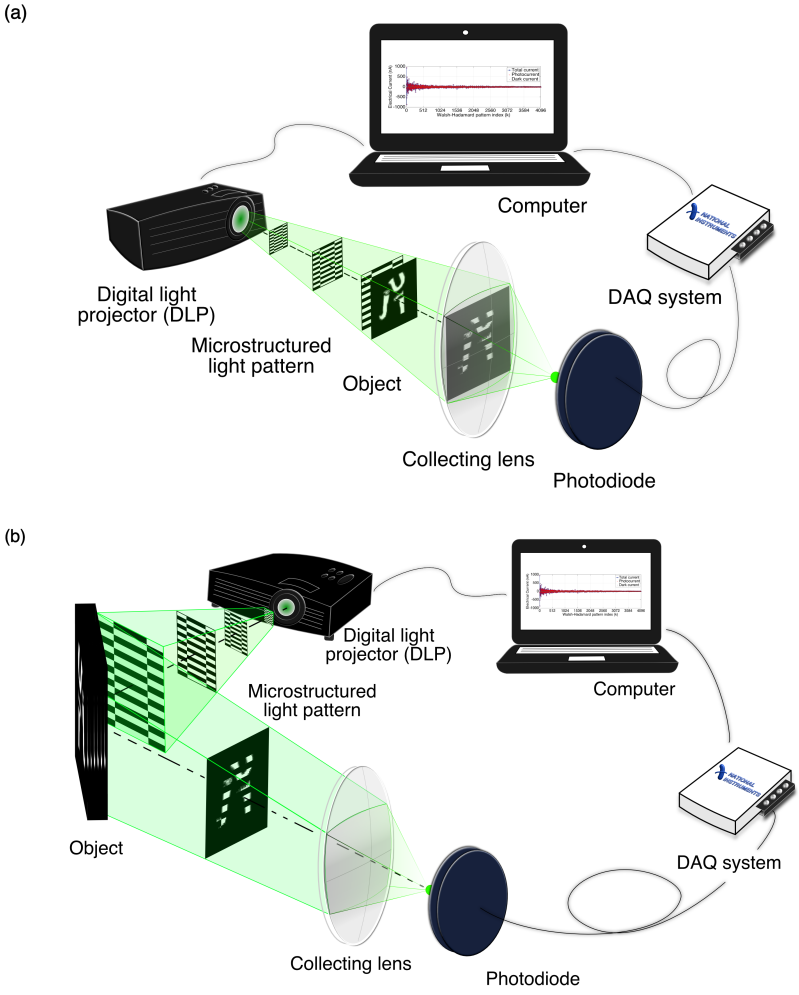

Figure 2.1: Schematic representation of the single-pixel camera working by (a) transmission and (b) reflexion.

In SPI technique, the image of the object $[O^*(n,m)]$ can be retrieved from the photodiode signal and the microstructured light patterns by using a simple linear superposition,

$$O^*(n,m) = \frac{1}{N \cdot M} \sum_{k=1}^{N \cdot M} I_{sp}^k \cdot \psi_k(n,m). \tag{2.2}$$

The most common types of SLMs are the liquid crystal spatial light modulator (LC-SLM) and the digital micromirror device (DMD) [45, 46]. In general, DMDs are used more frequently than LC displays in SPI applications, except when phase modulation is required, because they provide larger frame rates. A DMD is a microelectromechanical system that contains a pixelated display composed by millions of tiny switchable mirrors. Each mirror is able to tilt to either $\pm 12°$ with respect to the surface normal, which corresponds to *on* or *off* states, respectively (see Figure 2.2). In the last years, technology advances of DMDs have improved the performance of SPCs. For example, the DMD Discovery series recently developed by Texas Instruments (DLP Discovery $^{\text{TM}}$4100 Development Kit) has a resolution up to full HD (1920×1080 pixels) and pattern rates up to 32,500 Hz [47]. These advances have allowed developing SPI applications at video rates [32, 48].

In spite of the high frame rate of SLM based on DMDs, the measurement time (t_m) is still the main issue of SPCs. The measurement time can be given by [49]

$$t_m = K \cdot \left(\frac{1}{R_{SLM}} + t_r \right), \tag{2.3}$$

where $K = N \times M$ is the number of microstructured light patterns used

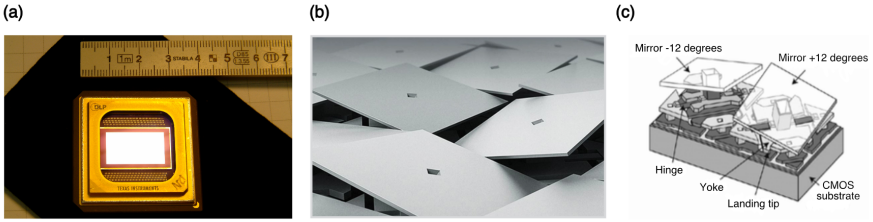

Figure 2.2: (a) Texas Instruments DLP digital micromirror device (DMD); (b) Micromirror arrangement on a DLP chip; and (c) A schematic structure of a single DMD micromirror (Extracted from [46, 50, 51]).

to sample the object, R_{SLM} denotes the pattern rate of the SLM, and t_r is the rise time response of the photodiode. Note that to reduce t_m, we must sample the object with a small number of patterns at high speed. Of course, increasing the DMD pattern rate means increasing its price. However, it is possible to decrease the number of patterns, and still reconstruct the image with high quality, by using compressive sampling (CS, also referred to as compressive sensing) techniques [52, 53] or adaptive methods [54, 55]. Currently, photodiodes respond at nanoseconds, hence the value of t_r does not represent a limitation in the measurement time of SPCs.

The mathematical functions used to sample the object by codifying the microstructured light patterns on the DMD are a key element in SPI techniques. The sampling functions commonly used in SPCs are speckle patterns, binary random distributions, noiselets [56], wavelets [57], Fourier [58], and particularly Walsh-Hadamard (WH) functions. In this research work, we selected the WH functions due to its attractive properties. These functions are real, symmetric and orthogonal. The WH functions constitute a basis that has associated a fast transformation and provide a good energy compaction for most natural images [59]. This last property makes them

excellent candidates for the use of CS methods. Moreover, WH functions have some advantages over Fourier ones in image coding [60].

The Hadamard transform is based on the Hadamard matrix ($\mathbf{H}$), which is a square binary array of ± 1's whose rows (and columns) are orthogonal to one another [60]. By definition, a normalized $n \times n$ Hadamard matrix satisfies the relation [61]

$$\mathbf{H}\mathbf{H}^T = \mathbf{I},$$

where $\mathbf{H}^T$ is the transpose matrix of $\mathbf{H}$, and $\mathbf{I}$ is the $n \times n$ identity matrix. To obtain Hadamard matrices of orden $n = 2^l$, we can use the Sylvester's construction [62]

$$\mathbf{H}_{2^l} = \mathbf{H}_2 \otimes \mathbf{H}_{2^{l-1}} = \frac{1}{\sqrt{2}} \begin{bmatrix} \mathbf{H}_{2^{l-1}} & \mathbf{H}_{2^{l-1}} \\ \mathbf{H}_{2^{l-1}} & -\mathbf{H}_{2^{l-1}} \end{bmatrix}$$

for $1 \leq l$, where $\otimes$ denotes the Kronecker product. As an example, the orthonormal Hadamard matrices of degree $n = 2, 4, 8$ are shown below:

$$\mathbf{H}_2 = \mathbf{H}_2 \otimes \mathbf{H}_1 = \mathbf{H}_2 \otimes 1 = \frac{1}{\sqrt{2}} \begin{bmatrix} +1 & +1 \\ +1 & -1 \end{bmatrix}$$

$$\mathbf{H}_4 = \mathbf{H}_2 \otimes \mathbf{H}_2 = \frac{1}{\sqrt{4}} \begin{bmatrix} +1 & +1 & +1 & +1 \\ +1 & -1 & +1 & -1 \\ +1 & +1 & -1 & -1 \\ +1 & -1 & -1 & +1 \end{bmatrix}$$

$$\mathbf{H}_8 = \mathbf{H}_2 \otimes \mathbf{H}_4 = \frac{1}{\sqrt{8}} \begin{bmatrix} +1 & +1 & +1 & +1 & +1 & +1 & +1 & +1 \\ +1 & -1 & +1 & -1 & +1 & -1 & +1 & -1 \\ +1 & +1 & -1 & -1 & +1 & +1 & -1 & -1 \\ +1 & -1 & -1 & +1 & +1 & -1 & -1 & +1 \\ +1 & +1 & +1 & +1 & -1 & -1 & -1 & -1 \\ +1 & -1 & +1 & -1 & -1 & +1 & -1 & +1 \\ +1 & +1 & -1 & -1 & -1 & -1 & +1 & +1 \\ +1 & -1 & -1 & +1 & -1 & +1 & +1 & -1 \end{bmatrix}$$

The number of sign changes along each row of the Hadamard matrix is called the *sequency* of the row. The Hadamard matrix generated from Sylvester's construction is not sequency ordered. However, it is possible to construct a Hadamard matrix of order $n = 2^l$ whose number of sign changes per row increases from 0 to $n-1$ [61]. Additionally, the row vectors of the Hadamard matrix can be considered a set of rectangular waves with a subperiod of $\frac{1}{n}$ units. These discrete functions are called Walsh functions and form a complete orthonormal basis for square integrable functions [59]. For this reason, the Hadamard matrix is also known as the Walsh-Hadamard (WH) matrix. As an example, a schematic representation of the matrix $\mathbf{H}_8$ and its Walsh functions are shown in Figure 2.3. The matrix was created directly by using Sylvester's construction. Note that, in principle, the rows are arranged in natural sequency [see Figure 2.3(a)]. Figure 2.3(b) shows the matrix $\mathbf{H}_8$ but with the rows arranged following an increasing sequency from 0 to 7. A profile of each row was plotted to represent graphically the frequency of each Walsh function. Note that the frequency depends on the sequency, as can be seen in Figure 2.3(d).

Two important practical questions should be considered when Hadamard matrices are used in SPI techniques. On the one hand, we need to codify

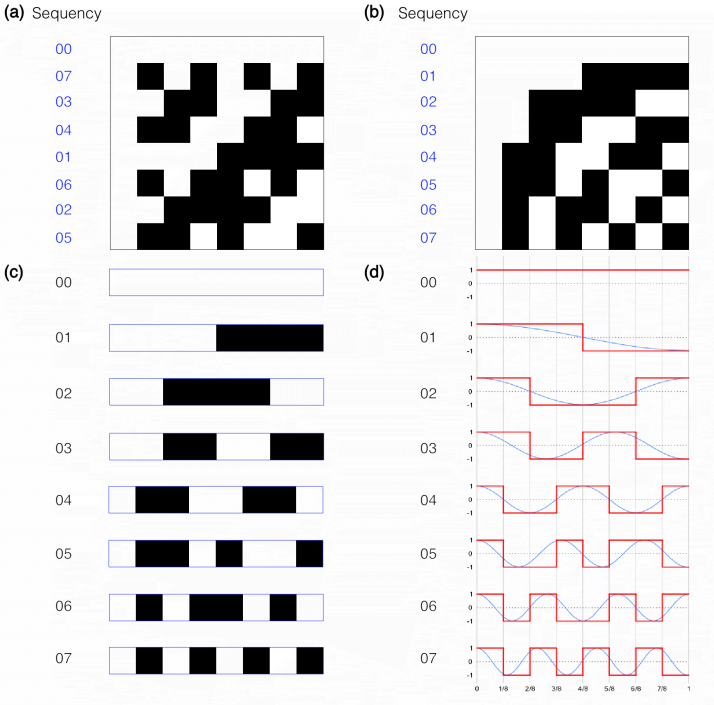

Figure 2.3: (a) Schematic representation of the Hadamard matrix of degree $n = 8$ in a natural sequency; (b) the matrix in (a) with rows ordered in increasing sequency from 0 to 7; (c) Walsh functions pertaining to the ordered matrix in (b); (d) profile of the Walsh functions in (c).

2-D sampling patterns in the SLM to perform 2-D imaging. To create these patterns, each Walsh vector that composes the Hadamard matrix $\mathbf{H}$ of degree n is reshaped into a $\sqrt{n} \times \sqrt{n}$ matrix, as is shown in Figures 2.4(a) and 2.4(b). In this thesis, these structured patterns will be called WH or Hadamard (H) patterns indistinctly. On the second hand, these functions are composed of values +1's and -1's. However, the DMD is able to codify only binary values 1 and 0, corresponding to states *on* and *off* of the mi-

cromirrors, respectively. To address this problem, each WH pattern ($\mathbf{H}_k$) can be considered to be composed of a positive ($\mathbf{H}_k^+$) and a complementary part ($\mathbf{H}_k^-$), fulfilling the following relation:

$$\mathbf{H}_k = \mathbf{H}_k^+ - \mathbf{H}_k^-, \tag{2.4}$$

where $\mathbf{H}_k^+ = \frac{\mathbf{H}_k + \mathbf{I}}{2}$ and $\mathbf{H}_k^- = \frac{\mathbf{I} - \mathbf{H}_k}{2}$ are complementary matrices, $\mathbf{I}$ is the identity matrix, and $k = 1, \ldots, n$ denotes the index of each WH pattern. The coefficient I_{sp}^k associated to each WH pattern is given by

$$I_{sp}^k = I_{sp}^{k^+} - I_{sp}^{k^-}, \tag{2.5}$$

where $I_{sp}^{k^+}$ and $I_{sp}^{k^-}$ correspond to the photodiode signal obtained from the positive and the complementary pattern, respectively. Figure 2.4(c) shows an example of the complementary WH patterns to be codified on the SLM.

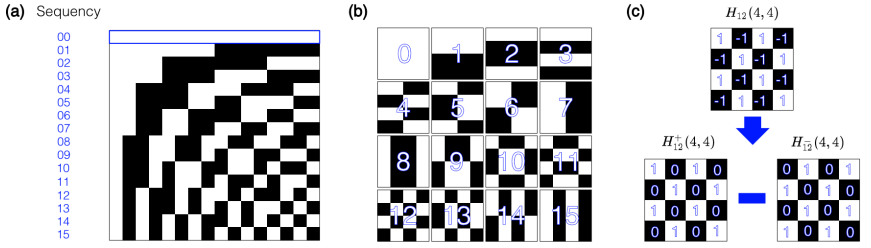

Figure 2.4: (a) Hadamard matrix of degree $n = 16$, whose rows follow a sequency order from 0 to 15; (b) a set of 16 WH patterns generated from the Hadamard matrix in (a); and (c) a schematic representation of the positive and the complementary component of the WH pattern with index $k = 12$.

2.2 The photodiode signal in SPCs

In SPCs, the image is computationally reconstructed from the electrical signal provided by the photosensor; in our case, a photodiode. In this context, the photodiode signal represents the inner product of the set of microstructured light patterns with the scene. Therefore, to analyze the quality of the image it is convenient to study the properties of the electrical signal provided by the photodiode as well as the sources of noise.

A photodiode is a semiconductor device that converts an optical signal into a current signal by electronic processes [63]. The electrical current of the photodiode is composed by two terms, the photocurrent (I_P) and the dark current (I_D). The first one is due to the photoelectric effect on the photodiode surface and it is given by [64]

$$I_P = R_\lambda \cdot P, \tag{2.6}$$

where P is the optical power level of the incident light and R_λ is the photodiode responsivity $[\frac{A}{W}]$. The second current is always present in the photodiode, even without illumination, and it is originated by the thermal generation of electron-hole pairs in the Si p-n and InGaAs p-i-n photodiode layers. Four different sources contribute to the dark current: the generation-recombination current in the depletion region, the diffusion current from the undepleted regions, the tunneling current, and the surface leakage current [65–67]. Nevertheless, the current-voltage of a p-n diode can be ideally described by the Shockley equation, which is given by [63]

$$I_D = I_s(T)\left[e^{\left(\frac{qV_A}{k_BT}\right)} - 1\right], \tag{2.7}$$

where $q = 1.602 \times 10^{-19}$ C is the electron charge, V_A is the bias voltage, $k_B = 1.381 \times 10^{-23}$ $\frac{\text{J}}{\text{K}}$ is the Boltzmann's constant, and T is the absolute temperature. Then, under the reverse-bias condition, the saturation current (as a function of the temperature T) can be written as

$$I_s(T) = C_n A_P T^3 e^{\left(-\frac{E_g(T)}{k_BT}\right)} + C_n A_P T^{\frac{3}{2}} e^{\left(-\frac{E_g(T)}{2k_BT}\right)}. \tag{2.8}$$

Assuming that the temperature is lower or close to room temperature, the first term in Eq.(2.8) can be considered negligible [63]. Taking this into account and substituting this expression in Eq.(2.7), the dark current is given by

$$I_D = C_n A_P T^{\frac{3}{2}} e^{\left(-\frac{E_g(T)}{2k_BT}\right)}\left[e^{\left(\frac{qV_A}{k_BT}\right)} - 1\right], \tag{2.9}$$

where C_n is a constant factor $\left[\frac{nA}{cm^2}\right]$, A_P is the photodiode area [cm^2], and $E_g(T)$ is the band gap energy of the photodiode material [eV] as a function of the temperature. The band gap energy $E_g(T)$ is described by the Varshni empirical relation for a Si p-n photodiode case [68]

$$E_g(T) = E_g^{Si}(0) - \frac{\alpha^{Si}T^2}{T + \beta^{Si}}, \tag{2.10}$$

and by the Sajal Paul relation for the $In_{1-x}Ga_xAs$ p-i-n photodiode case [69]

$$E_g(x,T) = E_g^{InAs}(0) - \frac{\alpha^{InAs}T^2}{T+\beta^{InAs}} + [E_g^{GaAs}(0) - \frac{\alpha^{GaAs}T^2}{T+\beta^{GaAs}} - E_g^{InAs}(0) + \frac{\alpha^{InAs}T^2}{T+\beta^{InAs}}]x - 0.475x(1-x), \quad (2.11)$$

where $E_g(0)$, α and β are material constants. Table 2.1 shows typical values of these parameters for Si and InGaAs materials [70, 71]. Therefore, when the photodiode is illuminated, the total current (I) at room temperature is given by

$$\begin{aligned} I &= I_P + I_D \\ &= R_\lambda \cdot P + C_n A_P T^{\frac{3}{2}} e^{\left(-\frac{E_g(T)}{2k_B T}\right)} \left[e^{\left(\frac{qV_A}{k_B T}\right)} - 1\right]. \end{aligned} \quad (2.12)$$

Table 2.1: Values of material parameters E_g, α and β

	$E_g[eV]$ at $T = 0K$	$\alpha[\frac{eV}{K}]$	$\beta[K]$
Si	1.1557	7.021×10^{-4}	1108
GaAs	1.519	5.405×10^{-4}	204
InAs	0.417	2.76×10^{-4}	93

In the single-pixel camera, the photocurrent and the dark current signals have an associated error due to the discrete nature of the electrical charge [72]. The noise of the former one is known as the photocurrent shot noise (σ_P) and it is given by

$$\sigma_P = \sqrt{2q\bar{I}_P B}, \tag{2.13}$$

where B is the noise bandwidth and $\bar{I}_P$ is the photocurrent mean value. The noise of the second current is called the dark-current shot noise (σ_D), defined as

$$\sigma_D = \sqrt{2q\bar{I}_D B}, \tag{2.14}$$

where $\bar{I}_D$ is the dark current mean value. Note that the photocurrent shot noise depends on the optical signal level and the dark-current shot noise does not. The sum of both noise values is known as shot noise (σ_{shot}) [64] and it follows the Poisson distribution statistics (commonly approximated by a Gaussian distribution when the current is large).

For the sake of completeness, we will consider the Johnson-Nyquist (or thermal) noise ($\sigma_{thermal}$), which is produced by the random thermal motion of electrons in a resistor, and it can be modeled as a stationary Gaussian random process (nearly white noise) [64]. The thermal noise is given by [63]

$$\sigma_{thermal} = \sqrt{\frac{4k_B T B}{R_{SH}}}, \tag{2.15}$$

where R_{SH} is the shunt resistance. Since σ_P, σ_D, $\sigma_{thermal}$ are linearly independent noise sources, and the total noise (σ_T) can be written as

$$\sigma_T = \sqrt{\sigma_P^2 + \sigma_D^2 + \sigma_{thermal}^2}. \tag{2.16}$$

Consequently, the signal-to-noise ratio (SNR) of the electrical current signal in units of decibels is defined as [64]

$$SNR = 10\log\left(\frac{\bar{I}_P^2}{\sigma_T^2}\right) = 20\log\left(\frac{\bar{I}_P}{\sqrt{2q\bar{I}_P B + 2q\bar{I}_D B + \frac{4k_B T B}{R_{SH}}}}\right). \quad (2.17)$$

2.3 Numerical model of SPCs

In this section, a numerical model of the SPC is described. The camera model takes into account the optical power level (P_{inp}) and the wavelength (λ_s) of the incident light, which is assumed to be a monochromatic light beam. It also considers the photocurrent, the dark current, the photocurrent shot noise, the dark-current shot noise, and the thermal noise as functions of the photodiode parameters.

The numerical process developed to simulate the SPC, from the moment in which the light source illuminates the DMD up to the image reconstruction (see Figure 2.1), is as follows:

Step 1 Obtain the number of photons per second ($\gamma_{inp}^{k^{\pm}}$) corresponding to the wavelength (λ_s) and to the optical power of the light (P_{inp}), arriving at the DMD,

$$\gamma_{inp}^{k^{\pm}} = floor\left(\frac{P_{inp}}{E_\gamma}\right), \quad (2.18)$$

where $E_\gamma = \frac{hc}{\lambda_s}$ is the photon energy.

Step 2 Distribute the $\gamma_{inp}^{k^{\pm}}$ photons spatially following a statistical Poisson distribution in a matrix $A(n, m)$

$$B^{k^{\pm}}(n, m) = \gamma_{inp}^{k^{\pm}} \cdot A(n, m), \tag{2.19}$$

where indexes n and m take values from 1 to N, respectively.

Step 3 Multiply the photon matrix $B^{k^{\pm}}(n, m)$ by $H_k^+(n, m)$, and $H_k^-(n, m)$, respectively,

$$C^{k^{\pm}}(n, m) = B^{k^{\pm}}(n, m) \cdot H_k^{\pm}(n, m). \tag{2.20}$$

Step 4 Calculate the number of photons per second ($\gamma_{out}^{k^{\pm}}$) that strike on the photodiode by projecting $C^{k^{\pm}}(n, m)$ onto the object $O(n, m)$ as a dot product,

$$\gamma_{out}^{k^{\pm}} = \sum_{m=1}^{N} \sum_{n=1}^{N} C^{k^{\pm}}(n, m) \cdot O(n, m). \tag{2.21}$$

Step 5 Obtain the optical power level ($P_{out}^{k^{\pm}}$) at the photodiode,

$$P_{out}^{k^{\pm}} = \gamma_{out}^{k^{\pm}} \cdot E_{\gamma}. \tag{2.22}$$

Step 6 Calculate the total current as the sum of the photocurrent and the dark current according to Eq.(2.12),

$$I^{k^{\pm}} = R_{\lambda} \cdot P_{out}^{k^{\pm}} + C_n A_P T^{\frac{3}{2}} e^{\left(-\frac{E_g(T)}{2k_B T}\right)} \left[e^{\left(\frac{qV_A}{k_B T}\right)} - 1 \right]. \tag{2.23}$$

Step 7 Obtain the noisy current ($I_{sp}^{k\pm}$) of the photodiode by adding the photocurrent shot noise, the dark-current shot noise and the thermal

noise to $I^{k^{\pm}}$. The noise terms are generated following a Gaussian distribution, taking into account Eqs.(2.13)-(2.15), respectively.

Step 8 Obtain the normalized photodetector signal related to $H_k(n,m)$ [taking into account Eq.(2.5)] as

$$I_{sp}^{k} = \frac{1}{I_0}\left(I_{sp}^{k^+} - I_{sp}^{k^-}\right), \tag{2.24}$$

where I_0 is the signal measured by the photodiode when the object is illuminated with the uniform pattern.

Step 9 Calculate the image $O^*(n,m)$ by a linear superposition of the Hadamard patterns weighted by the current signal of the photodiode as follows

$$O^*(n,m) = \frac{1}{N^2}\sum_{k=1}^{N^2} I_{sp}^{k} \cdot H_k(n,m). \tag{2.25}$$

2.4 Results

2.4.1 Numerical results

The numerical model described in the previous section was used to analyze the performance of a SPC using photodiode detectors under different circumstances. Three different studies were developed analyzing the image quality when: (1) the optical power level of the light source changes; (2) we use light sources with different wavelengths; and (3) the photodiode temperature varies. The simulations were performed for two commercial photodiodes, DET36A Thorlabs and DET10C Thorlabs, whose specifications are

shown in Table 2.2. Moreover, the dark current (I_D), the dark-current shot noise (σ_D), and the thermal noise ($\sigma_{thermal}$) curves are plotted as a function of the temperature (see Figure 2.5). The curves were obtained taking into account the Varshni empirical relation [Eq.(2.10)] for the Si detector case, and the Sajal Paul relation [Eq.(2.11)] for the InGaAs detector case. The material parameters are shown in Table 2.1.

Table 2.2: Photodiode parameters

Parameter		Silicon Biased Detector	InGaAs Biased Detector
Detector model		DET36A Thorlabs	DET10C Thorlabs
Photodiode active area	A_P	13.0 mm^2	0.8 mm^2
Wavelength range		350-1100 nm	900-1700 nm
Band gap energy at 298K	E_g	1.1114 eV	0.7379 eV
Rise time response	t_r	14.0 ns	10.0 ns
Noise bandwidth	B	0.025 nHz	0.035 nHz
Bias voltage	V_A	10.0 V	5.0 V
Saturation current at 298K	I_s	0.35 nA	1.0 nA
Shunt resistance	R_{sh}	1.0 GΩ	10.0 GΩ
NEP at λ_P		$1.6 \times 10^{-14} \frac{W}{\sqrt{Hz}}$	$2.5 \times 10^{-14} \frac{W}{\sqrt{Hz}}$

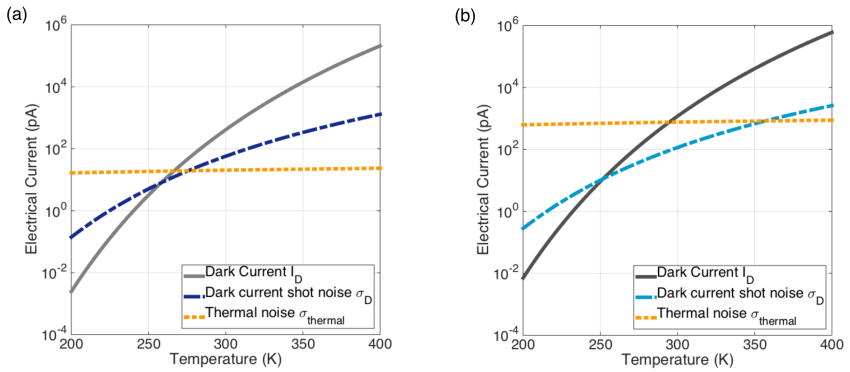

Figure 2.5: Simulated dark current, dark-current shot noise and thermal noise as a function of the temperature for (a) Si biased detector (DET36A Thorlabs) and (b) InGaAs biased detector (DET10C Thorlabs).

Firstly, we analyzed the image quality as a function of the optical power level of the light source. We fixed the wavelength of the light source to 520 nm and the photodiode temperature to 298 K. Figure 2.6 shows the photocurrent, the dark current, and the total current associated to the single-pixel camera for two different optical power levels; (a) 42.49 μW and (b) 0.0085 μW, respectively. We also show recovered images by applying SPI techniques to the different current signals in the plot. We can see that for the case of low light power in Figure 2.6(b), the photocurrent is noisier, the total current is worst, and therefore the quality of the image deteriorates with respect to the case in Figure 2.6(a).

We numerically evaluated the image quality using the SNR metric defined in Ref. [73]. The reference image is obtained by SPI techniques but using only the photocurrent values without considering the noise sources. We plot in Figure 2.7 the SNR as a function of the optical power of the light source. As expected, the image quality obtained by the SPC improves when the optical power increases. In the same figure, we also plot the curve of the SNR as a function of the optical power level measured from the photodiode signal. The reference signal is again the photocurrent signal without noise. Of course, the SNR is the same in both cases. Therefore we will use the SNR measured from the reconstructed images, from now onwards.

In the second numerical experiment, we analyzed how the wavelength of the light source influences the performance of the SPC. The optical power of the light source was set to 8.49 μW and the photodiode temperature to 298 K. Figure 2.8(a) shows the dependence of the SNR versus wavelength for the DET36A and the DET10C photodiodes. In Figure 2.8(c) we display several images reconstructed with our model for different wavelengths of the incident light. The key point to understand the relationship between the image quality and the wavelength is the photodiode responsivity (R_λ). In

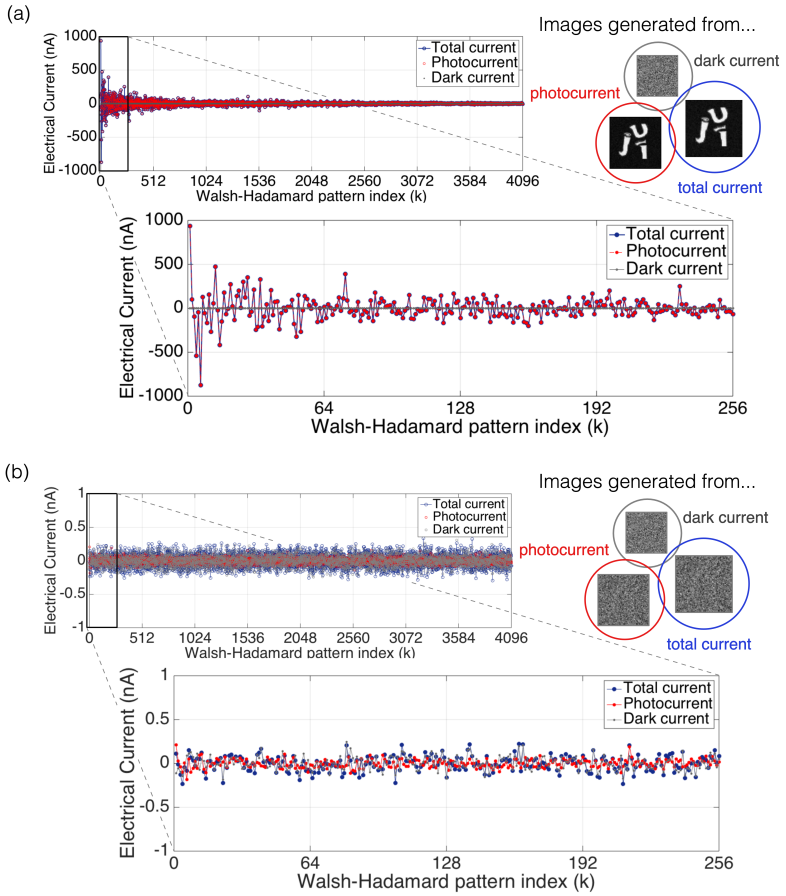

Figure 2.6: Photocurrent, dark current, and total current with their associated noise values as a function of the WH pattern index. Two different optical power values were considered (a) 42.49 μW and (b) 0.0085 μW. The wavelength of the light source was fixed at 520 nm and the photodiode temperature at 298 K. Images computed from these electric signals are shown on the right. In both cases, the resolution of the WH patterns is 64 $\times$ 64 pixels (Reprinted from [74]).

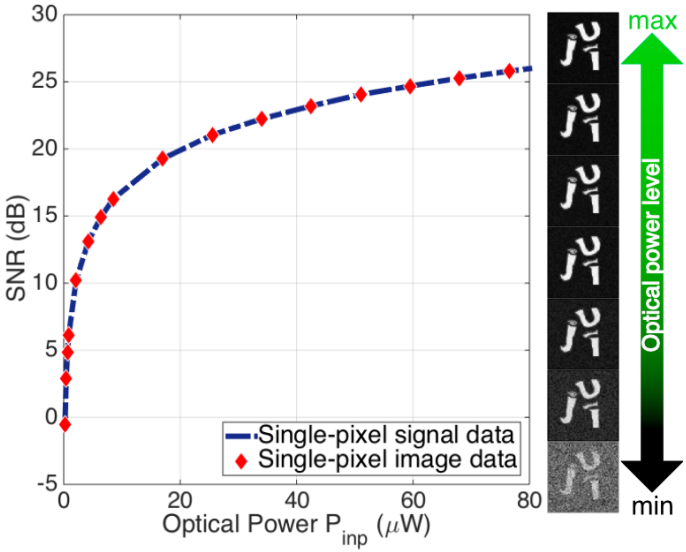

Figure 2.7: SNR of the signal and the recovered images as a function of the optical power P_{inp}. The recovered images on the right part are a set of samples corresponding to the red data points in the SNR curve (Reprinted from [74]).

a photodetector, the incident optical power and the generated photocurrent are proportionally related by the responsivity [Eq.(2.6)]. Therefore, the photocurrent increases as the responsivity rises up, although the optical power remains constant. The responsivity versus wavelength curves for both photodiodes are presented in Figure 2.8(b) [75,76]. As we can see comparing Figure 2.8(a) and (b), the behavior of the SNR and responsivity curves are closely related.

Finally, we analyzed the dependence of the image quality with the photodiode temperature. The wavelength of the light source was set to 520 nm and 1600 nm for the DET35A and the DET10C detectors, respectively. For each

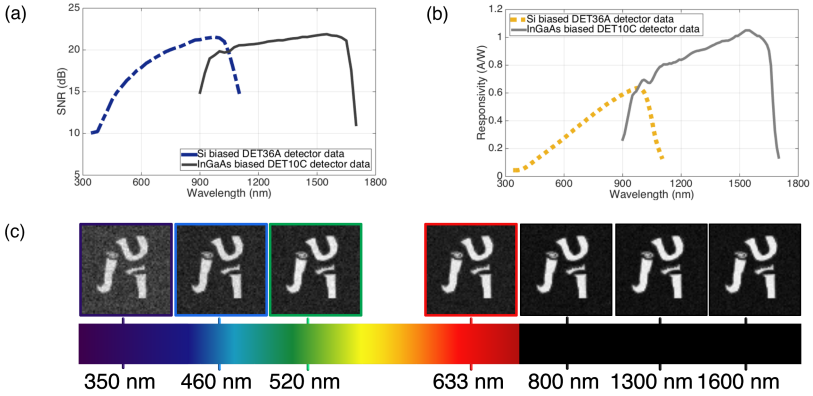

Figure 2.8: (a) SNR as a function of the wavelength of the light source; (b) responsivity data of both photodiodes [75,76]; and (c) recovered images for different wavelengths (Reprinted from [77]).

detector, three curves of the SNR as a function of the photodiode temperature are plotted for constant values of the optical power (42.49 μW, 8.49 μW and 0.21 μW) as shown in Figure 2.9. Moreover, several images for different values of temperature and optical power are displayed. In general, the SNR of the image decreases as the temperature increases. However, as we can see in the figure, the influence of the temperature on the SNR value is less significant for higher optical power levels. In particular, the performance of these photodiodes is suitable even with high temperatures whenever the optical power is higher than 8.50 μW. As previously shown in Figure 2.5, the dark current and the dark-current shot noise increase when the temperature increases. Although the current and its noise increase when the temperature increases, this effect is negligible in the SNR curves if the optical power level is high.

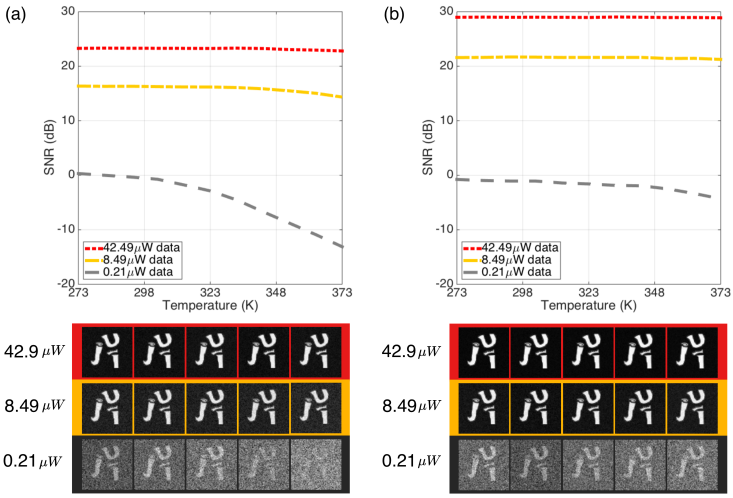

Figure 2.9: SNR dependence with the photodiode temperature for three optical power levels: 42.49 μW, 8.49 μW and 0.21 μW for (a) the Si biased detector (DET36A Thorlabs), and (b) the InGaAs biased detector (DET10C Thorlabs). The recovered images obtained for those optical power levels are shown as well. For those images, the temperature range starts at 273 K and ends at 373 K in 25 K steps (Reprinted from [77]).

2.4.2 Experimental results

A scheme of the experimental setup by using transillumination is depicted in Figure 2.10. In this case, a DMD (DLP Discovery 4100, Texas Instrument) was illuminated with a collimated light beam generated with an incoherent white-light source. A narrow band pass filter (P10-515-S 93819, Corion) centered at a wavelength of 520 nm with a bandwidth of 20 nm was used to avoid spectral artifacts. In order to apply SPI techniques, microstructured light patterns corresponding to 2-D functions of the orthonormal WH basis with 64×64 pixels were coded on the DMD display in a chip area of $1024 \times$

1024 micromirrors with a micromirror pixel pitch of 10.8 μm. The WH patterns were projected onto the object plane using a 4-f optical imaging system formed by two achromatic lenses L1 and L2. The focal distances of L1 and L2 were $f_1 = 100$ mm and $f_2 = 100$ mm, respectively. The magnification factor of the 4-f optical system was 1.0. Therefore, the field of view (FOV) was 1.10×1.10 cm, which is, in fact, the size of the WH patterns on the DMD display. Note that a circular diaphragm was used on the Fourier plane in order to filter unwanted diffracted orders produced by the periodic micromirror arrangement on the DMD. The light transmitted by the object was subsequently collected by lens L3 and focused onto a Si biased detector (DET36A Thorlabs) located at the back focal point of L3; $f_3 = 50$ mm. The optical power level of the incident light was adjusted by using a neutral density filter wheel (NDC-100S-4M-mounted step variable ND filter) located in front of the lamp and measuring power with a power meter (Coherent, FieldMaster GS) close to the photodiode sensor. Finally, the signal was digitized and saved in a computer by using a data acquisition system (NI-9215, National Instruments). The image was reconstructed by using Eq.(2.25). The object was a black and white logo of our university (UJI) printed in a transparent acetate slide. The object size was 1.10×1.10 cm with a total transmittance factor of 0.12. It should be mentioned that this object has the same features as the one used in subsection 2.4.1.

Figure 2.11(a) shows numerically and experimentally recovered images with different levels of the optical power. We can see that, in both cases, the noise level decreases with the optical power. This is corroborated by the results in Figure 2.11(b), which shows that the SNR curve corresponding to images obtained with the simulated and the experimental systems have a similar dependence with the optical power. This fact confirms the validity of our numerical model.

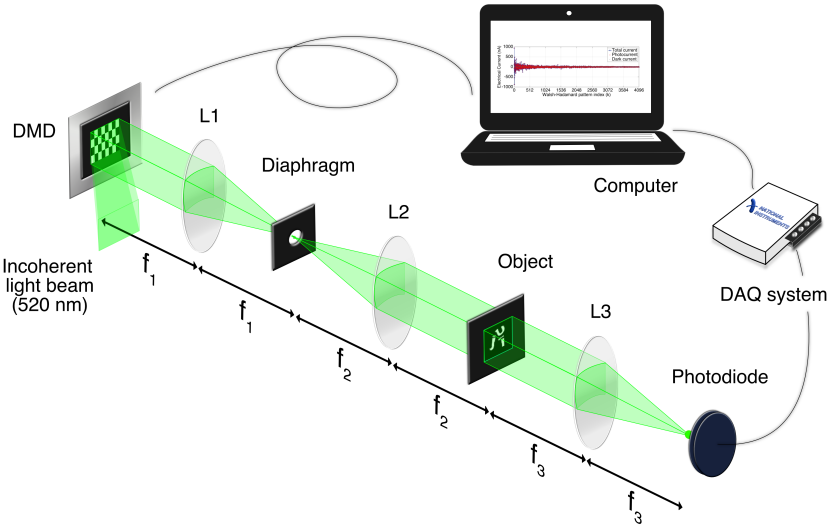

Figure 2.10: Experimental setup of the single-pixel camera (Reprinted from [74]).

However, even though the model has been developed taking into account the most important noise factors during the imaging process, there is still a discrepancy in the values of the SNR for the experimental and the simulated images. This difference is produced by several other noise sources not included in the model. First, we have considered that both the DMD reflectance and the object transmittance are ideal binary functions, which is not true in practice. Second, we did not introduce background, or ambient, light into the numerical model, with the unavoidable associated noise. Finally, we did not consider the current-to-voltage and the analog-to-digital conversion processes, which produce certain amount of noise. A clear example in the last case is the quantization noise.

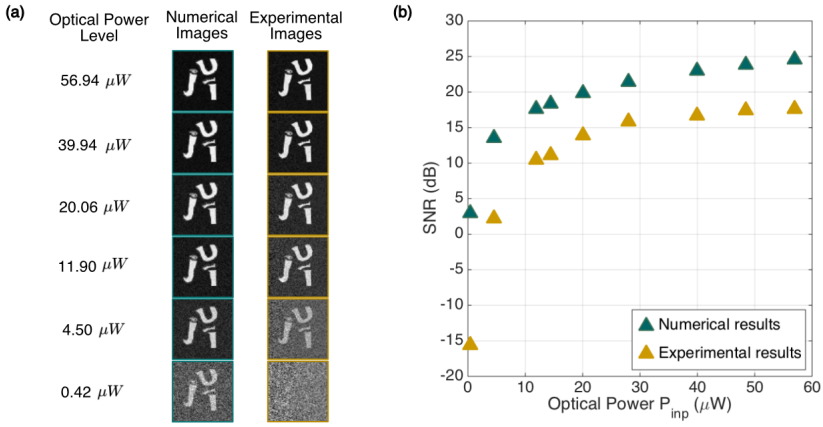

Figure 2.11: (a) Numerically and experimentally recovered images for different optical power levels P_{inp}; (b) SNR dependence with P_{inp} for the experimental and numerical images (Reprinted from [77]).

2.5 Summary

In this chapter, a numerical model of a SPC has been developed, considering the characteristics of the incident light and the physical properties as well as the specifications of the photodiode. We have accomplished a careful and rigorous mathematical review of the electrical behavior of Si and InGaAs detectors. Our model takes into account the photocurrent, the dark current, the photocurrent shot noise, the dark-current shot noise, and the Johnson-Nyquist (thermal) noise of two commercial photodiodes, a Si and an InGaAs detector.

Numerical simulations with our model have allowed us to analyze the behavior of the single-pixel imaging (SPI) technique in different contexts. In particular, we have studied the quality of the final image as a function of

the power of the light source. We have corroborated the reduction of the SNR for low light levels. We have also observed the clear link between the quality of the photocurrent signal and the quality of the reconstructed image. These results can be useful to predict the behavior of imaging systems working in low light level conditions.

We have also studied the dependence of the SNR with the wavelength of the light source. In this case, we conclude that the influence of the wavelength arises from the variation of the quantum efficiency and the responsivity of the photodetector. Such analysis could be the first step in the application of SPI techniques to multispectral imaging.

Finally, we have analyzed the quality of the images provided by the SPC as a function of the photodiode temperature. The study is performed for both a Si biased and an InGaAs biased detector. The main conclusion in this case is that the SNR of the reconstructed images changes only slightly with the temperature for high values of the light power. However, the reduction is clearly significant for low light levels. Therefore, cooling the detector can play an important role in photon counting or low light level applications.

An experimental SPC has been developed in order to validate the results provided by our model. The quality of the images obtained experimentally do not match perfectly with that predicted by the model. The discrepancy is due to several unaccounted sources of uncertainty such as non uniformities in the mirrors of the DMD or in the object substrate, as well as noise introduced in the signal amplification process or the analog-to-digital conversion procedure. However, we have shown that the quality of the final image, in terms of the SNR, changes in a similar way with the light power. This allows us to confirm that the model can be useful to predict the behavior of SPI systems based on photodiodes under different circumstances.

Chapter 3

Imaging through scattering media by Fourier filtering

Imaging through scattering media has been a longstanding issue in many applications in science, mainly in biomedical imaging. Accordingly, different optical approaches have emerged to retrieve the information of objects hidden in highly scattering media, which can be classified as a function of the regime of light used to reconstruct the image. Techniques based on the directionality of the unscattered (or ballistic) light are an example of the most successful techniques. These techniques provide better resolution although, of course, paying the price of low penetration depth. In this context, Fourier filtering is a practical and effective technique that allows the reduction of scattered light in conventional imaging systems. However, the use of a spatial filter also blocks high frequencies reducing the spatial resolution of the final image. In fact, there is a tradeoff between image resolution and contrast inherent to this technique. In this chapter, we show how this tradeoff can be overcome by combining Fourier filtering and SPI methods.

In the following sections, firstly, a brief description of light scattering is made. Second, an experimental SPC to analyze the influence of Fourier spatial filtering on SPI techniques is developed. Third, structured illumination techniques with a CMOS image sensor are combined to perform SPI with Fourier filtering techniques in a flexible way. Next, single-pixel imaging (SPI) techniques with Fourier filtering are applied to recover the image of an object hidden behind a turbid medium. Finally, the main conclusions are summarized.

3.1 Light scattering

When light travels through a turbid medium, we can distinguish three main components in terms of the degree of interaction of the photons with the medium: diffusive, snake and ballistic. The diffusive component of light consists of photons scattered randomly by the medium. The snake component is formed by photons that propagate along zigzag paths slightly deviated from the straight path. Photons that are not scattered but follow a straight line through the medium are called ballistic. This is an important light component in imaging applications because it carries very relevant information about objects inside or behind the scattering medium [3,9]. In a highly scattering medium, the diffusive component of the light is much stronger than the snake and ballistic components. A good estimate of the amount of ballistic light transmitted through a turbid medium is given by the Beer-Lambert law [78]. According to this law, we have:

$$I_T = I_0 e^{-\mu_e \cdot d}, \tag{3.1}$$

where I_0 is the input light intensity, supposed perfectly collimated, d is the thickness of the turbid medium, and $\mu_e = \mu_s + \mu_a$ is the extinction coefficient [cm^{-1}]. The parameters μ_s and μ_a are the scattering coefficient and the absorption coefficient, respectively. The extinction coefficient can be related to the mean-free path length (l) as follows:

$$l = \frac{1}{\mu_e} = \frac{1}{\mu_s + \mu_a}, \tag{3.2}$$

where l [cm] is defined as the average distance that a photon travels between two consecutive scattering events in an isotropic medium [2]. However, if the medium is anisotropic, i.e., if light propagates in a preferred direction, is better to consider the transport mean-free path [cm], usually referred to as l^* or l_{tr} (we chose the notation l^*), defined as [79]

$$l^* = \frac{1}{\mu_s(1-g) + \mu_a}, \tag{3.3}$$

where $g = \langle \cos\theta \rangle$ is the dimensionless factor of the anisotropy, and $\langle \cos\theta \rangle = \int_0^{2\pi} \sigma(\theta) \cos(\theta) d\theta$ is the average of the cosine of the scattering angle θ taking into account the dependence of the scattering cross section σ with θ [80]. In the macroscopic scale, g quantifies the anisotropy of scattering, for instance, in biological tissue g is typically 0.7-1 [81]. Note that for the isotropic case, when light propagates uniformly in all directions, $\langle \cos\theta \rangle = 0$, $g = 0$, and consequently $l^* = l$.

Imaging in the presence of light scattering is a problem that can be addressed from many different approaches. They can be classified in terms of the depth of penetration measured in l^* units [2, 82, 83]. In the macroscopic

regimen, when light has traveled more than $10\,l^*$, diffuse optical techniques such as diffuse optical tomography (DOT) are used to retrieve information through highly scattering media [84]. In the mesoscopic regime, for depths from l^* to $10\,l^*$, techniques based on the control of light wavefronts with spatial light modulators (SLM) have allowed recently to performing imaging with good resolution [85, 86]. Finally, in the microscopic regimen, when light travels depths smaller than $1\,l^*$, the information to perform imaging is extracted directly from the directionality of the ballistic light. A schematic representation of these regimes as a function of the distance in l^* units is shown in Figure 3.1.

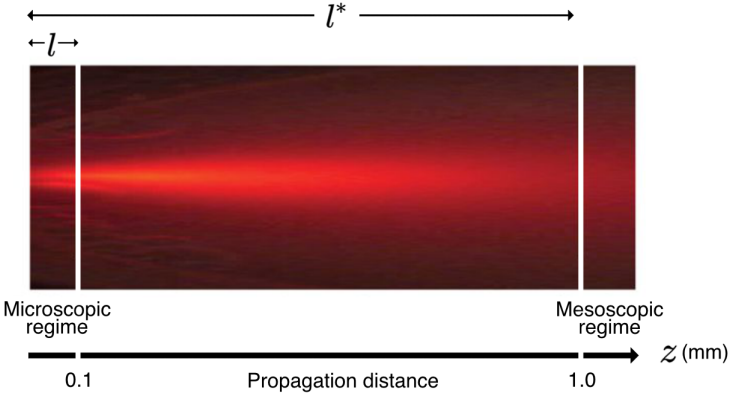

Figure 3.1: Schematic representation of scattering light regimes as a function of the penetration depth in transport mean free path (l^*) units. The scale depends on the optical properties of the medium and the wavelength of the incident light (Adapted from [2]).

Ballistic approaches that use coherence [87,88], temporal [3], or spatial gating [10] have proven to be the best options to obtain higher resolutions imaging although, of course, at low penetration depths. For instance, time-gating techniques select ballistic photons from light pulses by taking into account

that they arrive earlier than the snake and diffuse photons to the detector [3]. Other techniques are based on the fact that the ballistic, snake and diffuse photons can be separated spatially by performing an optical Fourier transformation as is shown in Figure 3.2. Fourier filtering is a practical and effective technique that, combined with ultrafast time-gating imaging, has allowed reduction of the scattered light by 10 orders of magnitude [9]. Recently, high-contrast images through scattering media have been obtained employing both Fourier filtering and structured illumination [10]. However, the use of a spatial filter to reduce the scattered light limits the achievable spatial resolution of the final image because high frequencies of the object are also blocked. In fact, there is a tradeoff between image resolution and contrast inherent to this technique.

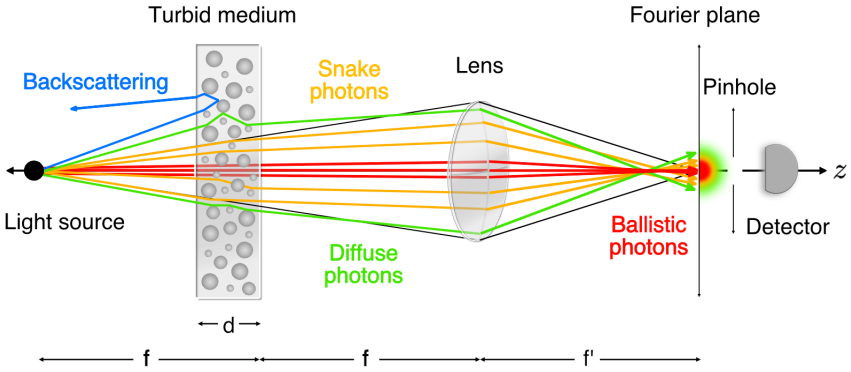

Figure 3.2: Diagram of the Fourier filtering technique. When light travels through a turbid medium the ballistic, snake, and diffuse photons are spatially separated on the Fourier plane. The ballistic and snake photons are located close to the center of the zero order of the Fourier transformation, while diffuse photons are far from the zero order. It is possible to block the diffuse photons by using a pinhole located at back focal plane of a lens as is shown in the scheme.

3.2 Single-pixel imaging with Fourier filtering

The experimental configuration to study the performance of the SPC with Fourier filtering is shown in Figure 3.3(a). The microstructured light patterns are generated with a DMD illuminated with a monochromatic collimated light beam. An optical system in a 4-f configuration, constituted by lenses L1 and L2, projects the patterns onto the object. A circular diaphragm is used to filter unwanted diffracted orders produced by the periodic micromirror arrangement on the DMD. Light transmitted by the object is collected by lens L3 and focused onto a PMT. A pinhole with variable diameter located at the back focal plane of L3 performs the spatial frequency gating. With the aim of comparing, we use a second experimental setup constituted by a conventional 4-f imaging system, formed by lenses L3 and L4, and a digital camera, as is shown in Figure 3.3(b). Specifically, the light beam is generated with an incoherent white-light source (HPLS200, Thorlabs), and an interference filter (P10-515S 93819, Corion) with a bandwidth of 20 nm centered at 520 nm. The DMD (DLP Discovery 4100, Texas Instrument) is a chipset array constituted by 1920×1080 micromirrors with a pixel pitch of 10.8 μm. The patterns codified on the DMD are 2-D functions of the orthonormal WH basis. Due to the binary modulation nature of the DMD, each WH function is projected combining two patterns, one codifying the positive and another the negative component of the function, as was shown in section 2.1. These functions are projected onto the object at a frame rate of 20 Hz. The focal distances of L1, L2, and L3 are the same, $f_1 = f_2 = f_3 = 100$ mm, while that of L4 is $f_4 = 75$ mm. The detector in Figure 3.3(a) is a photomultiplier tube (PMM01, Thorlabs Inc.) and the sensor in Figure 3.3(b) is a digital camera (UI-1540SE-M-GL, IDS) with a CMOS image sensor of 1280×1024 pixels with a pitch of 5.2 μm. The

magnification factor of the 4-f optical system in Figure 3.3(b) is 0.75. The object in both arrangements is a sector star target R1L1S2P that contains 36 radial sector pairs.

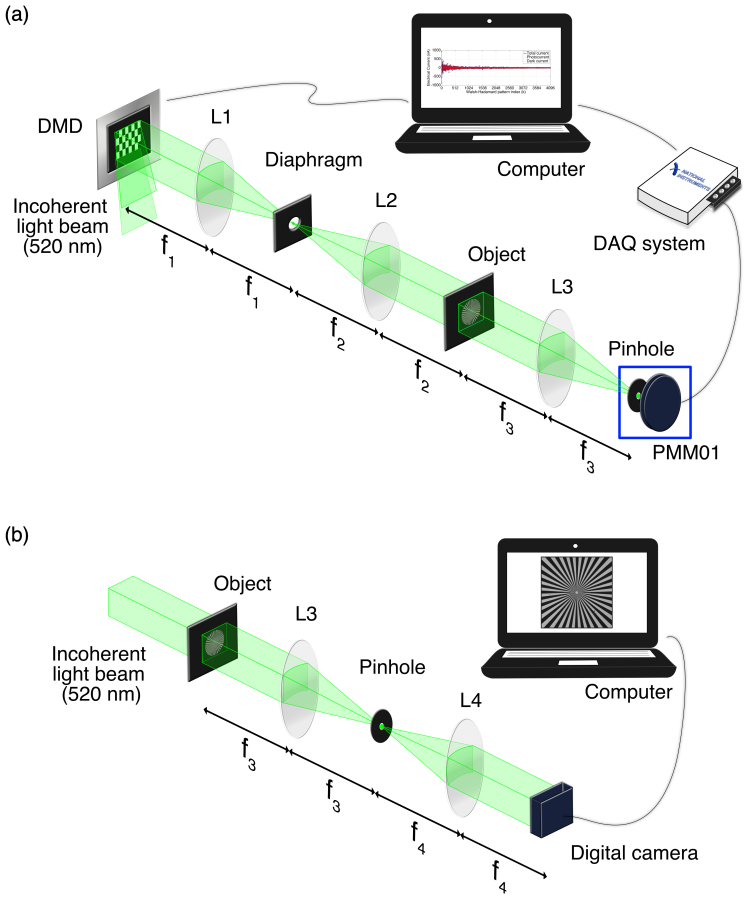

Figure 3.3: Schematic diagram of (a) the single-pixel camera, and (b) the conventional imaging setup (Reprint from [36]).

To operate with the SPC obtaining the maximum resolution and a wide field of view (FOV) in the shortest possible measurement time, we adopt the following strategy. We project different sets of microstructured patterns, all of them with a low number of pixels but with different sizes, adapting the spatial resolution of the sampling patterns to that of the object. Our approach is related with supersampling methods that use signal processing techniques to obtain high-resolution images from multiple low-resolution samples [55,89]. In particular, we project four sets of WH patterns each one consisting of 64×64 pixels codifying the full collection of 4096 WH functions for this resolution as is shown in Figure 3.4(a). Each pixel of the pattern is codified with a number of micromirrors that varies from 8×8, for the set with lower spatial resolution, to 1×1, for the patterns with higher spatial resolution. By projecting these patterns onto the object, and reconstructing the images with SPI techniques, we obtain four elemental images with 512×512, 256×256, 128×128, and 64×64 pixels [see Figure 3.4(b)]. The final image of the object is generated by combining the previous images into a single one, overlapping digitally the images with higher resolution over those with lower resolution, as is shown in Figure 3.4(d). Using this strategy, we recover an image with 512×512 pixels, with the maximum spatial resolution at the center, where the object has the smaller details, and lower spatial resolution at the borders. The number of projected patterns and, accordingly, the measurement time, is reduced by a factor of 16, equal to the ratio of 512×512 to $4 \times 64 \times 64$. In our case, the reconstruction time is $\sim$ 14 min ($\sim$ 0.8 s by using a fast DMD working at 20 kHz). Of course, the method is adjusted to the sector star target, but it will be easy to adapt it also to other objects with non homogeneous resolution.

To evaluate the influence of Fourier filtering on SPI, we plot the Michelson contrast, or visibility, as a function of the spatial frequency. The numerical

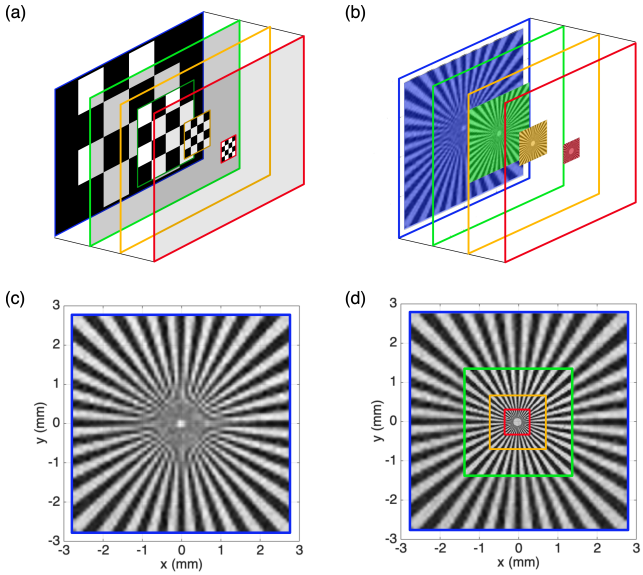

Figure 3.4: Experimental results obtained with the single-pixel camera setup: (a) Hadamard patterns with 64×64 pixels of different size codified on the DMD with different number of micromirrors; (b) images of the sector star target with different spatial resolution recovered with the patterns in (a); (c) low resolution image with 512×512 pixels [image marked blue in (b)]; (d) final image with 512×512 pixels obtained by digital combination of images in (b) (Reprint from [36]).

process to calculate the contrast is as follows (see Figure 3.5). First, the four elemental images constituting the final image are considered. Second, we sample each elemental image at different spatial frequencies (f_{r_1}) by using ring masks with different internal radius (r_1), as is shown in Figures 3.5(b) and 3.5(c). Third, the gray levels of the sampled ring are represented in polar coordinates as can be seen in Figure 3.5(d). The vertical axis denotes the radial coordinate while the horizontal axis represents the arc length, both in mm. To calculate the Michelson contrast, the maximum (I_{max})

and minimum (I_{min}) values are determined from the profile of intensity values obtained by averaging the values along the radial coordinate [see Figure 3.5(e)]. Finally, the Michelson curve as a function of the spatial frequency is plotted for each elemental image as is shown in Figure 3.5(f). The threshold of the spatial frequency, associated to the pixel size of the specific WH pattern codified on the DMD, is marked with a vertical color line for each curve. For our SPC, the highest spatial frequency is 46.29 line-pairs/mm. The solid black curve in Figure 3.5(f) shows the Michelson contrast corresponding to the final image in Figure 3.5(a). This is the curve that will be used for different filtering conditions from now onwards.

To study experimentally the influence of Fourier filtering on SPI, and compare it with the case of Fourier filtering in conventional imaging, we use a pinhole with variable diameter at the back focal plane of lens L3 in both optical systems in Figure 3.3. The experimental results are shown in Figure 3.6. Images in the first row of Figure 3.6(a) were obtained with the SPC, while those in the second row were recorded with the conventional one. Images on each column correspond to different Fourier filtering conditions: no pinhole for the first column and pinholes with a diameter of 2.0, 1.0, 0.3, and 0.2 mm for the subsequent columns, respectively. Note that by reducing the pinhole diameter, the contrast remains approximately constant in the SPI approach, even for small pinhole diameters. In this case, the loss in resolution is negligible. On the contrary, the loss is quite noticeable in the conventional imaging system as the pinhole diameter decreases. These experimental results are corroborated by plotting the Michelson contrast as a function of the spatial frequency. Figures 3.6(b) and 3.6(c) show the results for the SPC and the conventional camera, respectively.

The key point to understand the behavior of SPI techniques under Fourier filtering is in the measurement process. As we have seen in section 2.1,

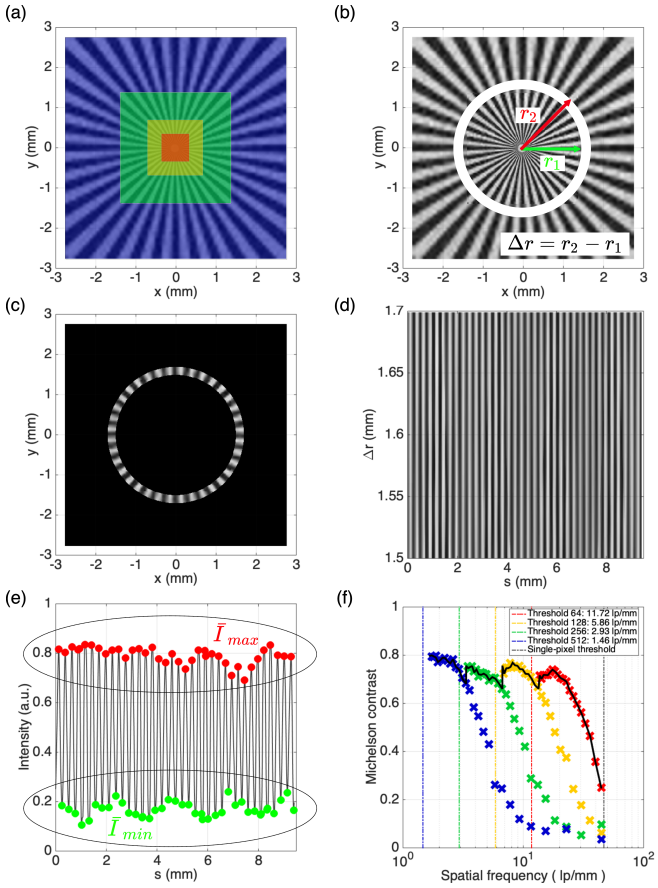

Figure 3.5: Schematic representation of the numerical process to obtain the Michelson contrast versus the spatial frequency: (a) final image formed by four elemental images; (b) the ring mask with internal radius r_1 from the star center; (c) area of the image sampled by the ring mask in (b); (d) representation of the ring in (c) in polar coordinates; (e) profile of the intensity values in (d); (f) curve of the the Michelson contrast versus the spatial frequency for each elemental image in (a). The black envelope curve shows the contrast of the final image.

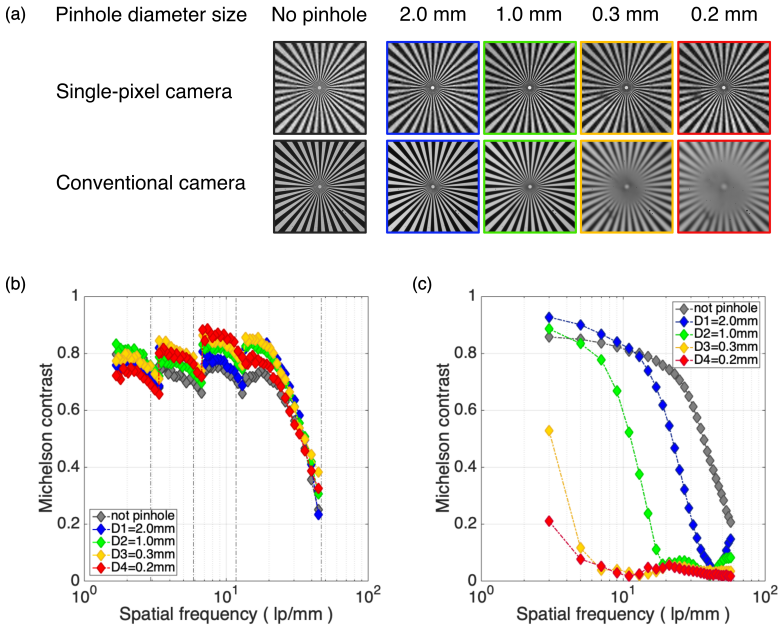

Figure 3.6: Experimental results obtained with the optical systems in Figure 3.3 and Fourier filtering techniques. (a) Images recorded by both cameras and different size of the pinhole diameter on the Fourier plane. Michelson contrast versus spatial frequency for (b) the single-pixel camera and (c) the conventional imaging system.

the image is reconstructed by measuring the projection of the object onto a set of test functions, in our case functions of the WH basis. Note that full information about this projection is contained in just the zero order of the Fourier transform of the sampled object. This is because the zero order provides the spatial average of the function being transformed, as can be verified from the expression of the Fourier transform with spatial frequencies equal to zero. Therefore, the object is still obtained by a simple linear

superposition of the functions of the basis with the measured coefficient, even if we filter all frequencies except the zero order at the Fourier plane of the detection side of the camera. The only effect of the filtering process is a reduction of the light power efficiency. It should be mentioned that the previous result will be different by doing an equivalent low-pass filtering in the illumination side of the SPC, but this is not the case of our study.

3.3 Digital Fourier filtering

The complementary metal oxide semiconductor (CMOS) image sensor is a device formed by a matrix array of light detectors. As is well know, these sensors transform the spatial light distribution of the incident light beam into a spatial distribution of electrical charges that can be measured and digitized by means of electronic circuits. In general, CMOS image sensors have a high sensitivity, work at high frame rates, and provide images with a high SNR. In this section we will take advantage of these properties of CMOS sensors to perform single-pixel imaging with a digital Fourier filtering technique. In particular, we combine sampling techniques using structured light patterns, typical of the SPCs, with light detection by using a digital CMOS camera.

The experimental configuration is depicted in Figure 3.7(a). As in the previous experimental setup [Figure 3.3(a)], a 4-f optical system, formed by lenses L1 and L2, projects the WH patterns onto the object. The light transmitted by the object is collected by lens L3 and focused onto a digital camera (UI-1540SE-M-GL, IDS), which is located at the back focal plane of lens L3. The focal distances of L1, L2 and, L3 are $f_1 = f_2 = f_3 =$100 mm.

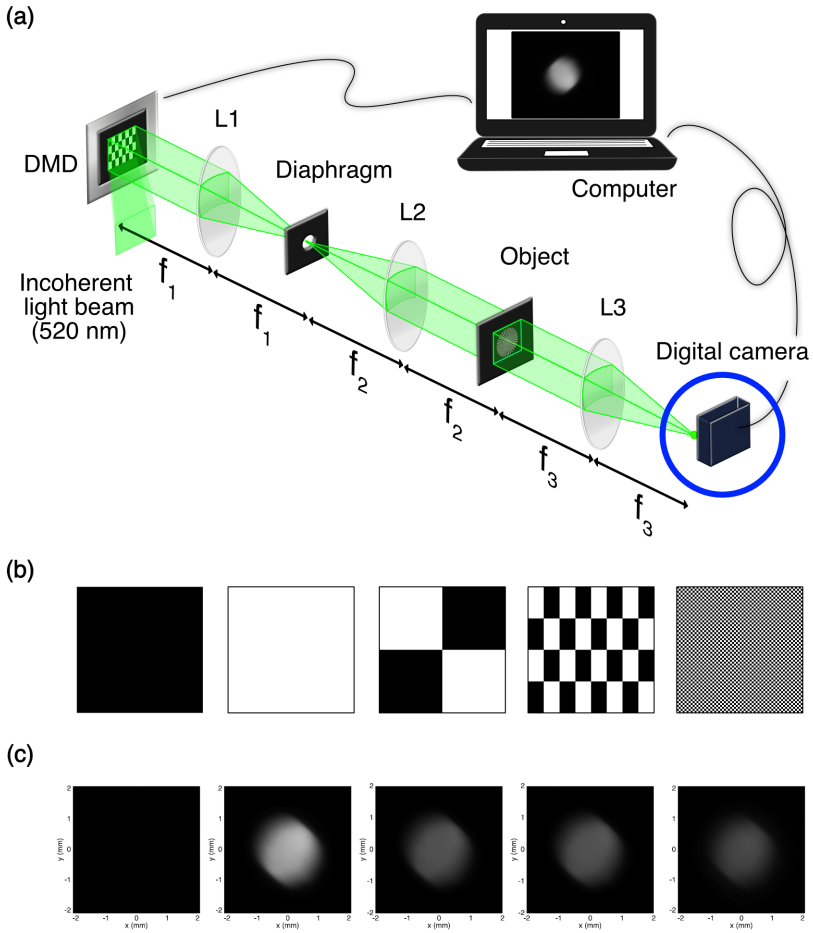

Figure 3.7: (a) Experimental setup of the single-pixel camera using a digital camera as bucket detector; (b) examples of the set of WH patterns projected onto the object plane; and (c) images of the zero order of the Fourier transform associated to the WH patterns in (b) obtained with the digital CMOS camera.

The digital camera contains a CMOS image sensor composed by a matrix array with 1280×1024 pixels, with a pixel pitch of 5.2 μm. The digital micromirror device and the digital camera are synchronized. In this way, we are able to take an image of the light distribution at the focal plane for each WH pattern codified on the DMD. In Figure 3.7(c) we show images of the zero order of the Fourier transformation for different sampling patterns. In this configuration, the coefficient associated to each sampling pattern is proportional to the light intensity integrated by an area of the CMOS sensor. As in the conventional SPI techniques with photodiodes, the image is reconstructed by a linear superposition of the WH patterns weighted by the corresponding coefficients. To perform the digital Fourier filtering operation, we use digital circular masks with different diameters to filter spatially the zero order of the Fourier transform as is shown in Figure 3.8.

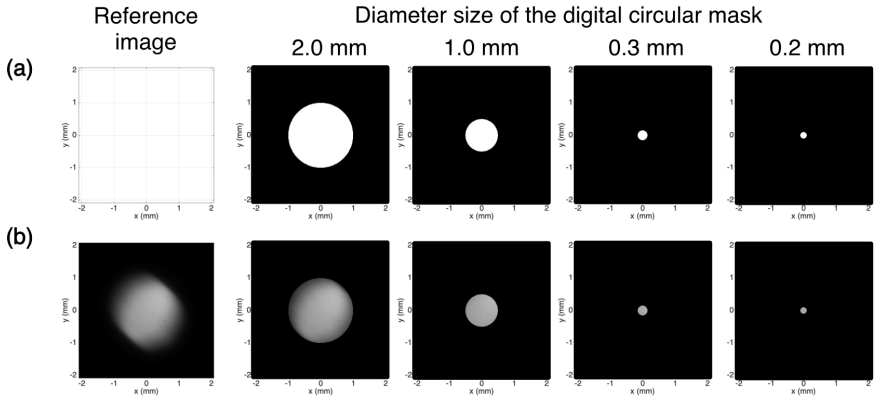

Figure 3.8: (a) Digital circular mask with different diameter sizes; (b) zero order of the Fourier transform corresponding to the uniform WH pattern filtered with the digital circular masks in (a).

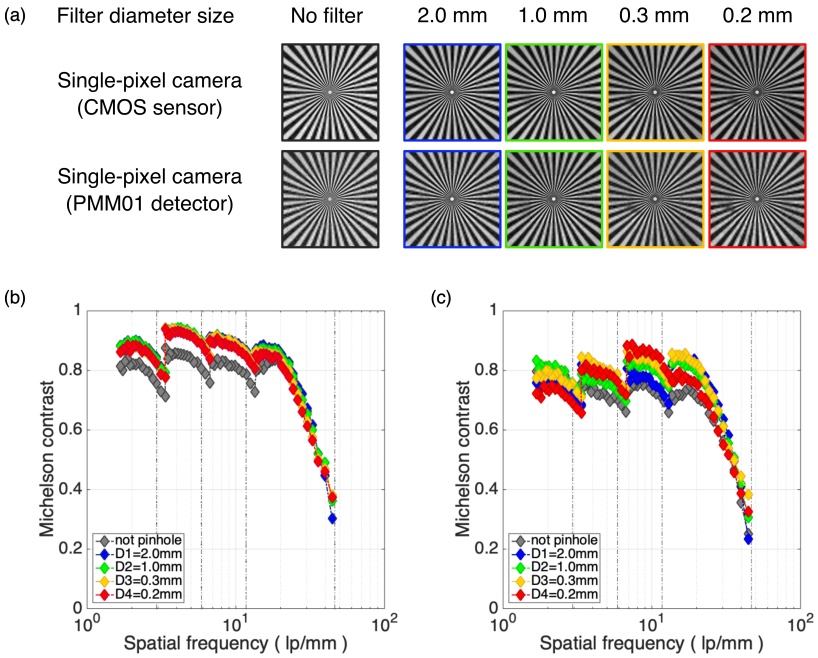

Figure 3.9: (a) Experimental images obtained with a SPI setup. In the first row, we show images obtained with a CMOS image sensor and the digital Fourier filtering technique. In the second one, we show those recovered with a PMT sensor and the pinhole Fourier filtering technique; (b) and (c) are plots of Michelson contrast curves versus the spatial frequency of the images in (a).

The experimental results are shown in Figure 3.9. Images in both rows of Figure 3.9(a) were obtained using a SPC arrangement. However, the images in the first row were obtained by using the CMOS image sensor as a bucket detector and the digital Fourier filtering technique, while those in the second row were obtained by using a PMT detector and filtering in the Fourier plane with a pinhole with variable diameter. Images on each

column correspond to different Fourier filtering conditions: no spatial filter for the first column and filter with a diameter size of 2.0, 1.0, 0.3, and 0.2 mm for the subsequent columns, respectively. To compare the quality of the images obtained with both techniques, we plot the Michelson contrast as a function of the spatial frequency in Figures 3.9(b) and 3.9(c). Note that the curves of contrast do not depend with the size of the circular filter when performing the Fourier spatial filtering, even for small diameters. Moreover, comparing the curves in both Figures, we conclude that the results of the digital Fourier filtering performed with the CMOS image sensor are similar but slightly better than their counterparts. The reason is, probably, the excellent sensitivity and SNR provided by a high-quality CMOS camera when many pixels collaborate together to record the intensity signal with the proper dynamic range. Furthermore, the alignment of the camera and the subsequent application of a digital filter is easier than the alignment of the PMT with the pinhole for each sequence of measurements.

3.4 Imaging through scattering media

A relevant application of Fourier filtering is on imaging through scattering media. It has been used to reject scattered light, thus increasing the proportion of ballistic light and, consequently, the image contrast [9,10]. However, this technique may also degrade the image quality, because the spatial-frequency gating operation will reduce also the spatial-frequency bandwidth of the final image. In view of the results obtained in sections 3.2 and 3.3, we propose to combine SPI techniques with Fourier spatial filtering to increase the quality of the images of an object hidden behind a scattering medium in a transmission configuration.

To study the validity of the approach, we locate a turbid slab against the object in the SPI arrangements shown in Figure 3.3(a), and Figure 3.7, respectively. The influence of the location of the scattering medium in the SPC has been widely discussed in Refs. [11,12,24]. It has been proved that a turbid medium located between the object and the sensor, at the detection side of the optical system, has no influence on the quality of the image. This is because the quality of the final reconstruction depends only on the properties of the projection of the sampling patterns onto the object plane. On the other hand, if the turbid medium is located between the DMD and the object, at the illumination side, the microstructure of the light patterns projected onto the object is degraded by scattering, worsening the quality of the reconstructed image. In this case, of course, the image quality depends on the scattering properties of the medium.

In our study, we located the scattering medium at the illumination side, the worse condition for SPI techniques. Again, we use a spatial filter with variable diameter at the back focal plane of lens L3, now to block the diffused photons and detect only the ballistic ones. For comparison, we repeated the experiment with the conventional system in Figure 3.3(b). In this case, the turbid slab was located at the detection side, as in Ref. [10]. It should be noted that by applying the Helmholtz reciprocity principle of reversibility of light, the single-pixel camera and the conventional one are equivalent locating the scattering medium at different sides of the object. However, the introduction of the spatial filter at the detection side, which is necessary to filter the scattered photons, breaks the symmetry.

As scattering medium, we use a turbid slab with a thickness of 3.7 mm and a coefficient of extinction of $\mu_e = 29.84$ cm^{-1}. The slab was made using epoxy resin, as substrate, and TiO_2 microparticles, as scattering agent, following the recipe in Ref. [90]. We mixed 0.725 (g/l) of TiO_2 rutile powder

(Titanium IV oxide, rutile powder, <5 μm particle size, Sigma Aldrich) with a 1:2 ratio of hardener (component B) to epoxy resin (component A) as is shown in Figure 3.10.

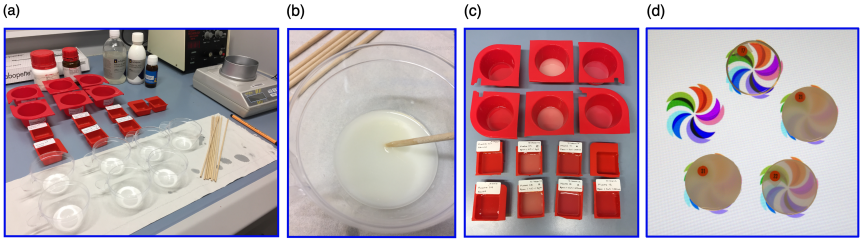

Figure 3.10: Process to make scattering phantoms with different thickness and scattering coefficient: (a) materials; (b) epoxy resin and TiO_2 microparticles mixture; (c) drying process; and (d) final results of the scattering samples (Reprint from [90]).

The experimental results with the scattering medium are shown in Figure 3.11. Images in the first and the second row in Figure 3.11(a) were obtained using the SPC arrangements shown in Figure 3.3(a), and Figure 3.7, respectively. Images in the first row were obtained using a CMOS image sensor as bucket detector in a SPI configuration, whereas images in the the second row were recovered using a PMT detector. To compare the performance of our SPI systems with that of a conventional imaging one, we show in the third row the images obtained by using the optical imaging setup shown in Figure 3.3(b). As in the previous sections, images on each column correspond to different Fourier filtering conditions.

Based on the comparison of the images in the first column with those in the second one in Figures 3.11(a), it can be concluded that the introduction of Fourier spatial filtering improves the image contrast of all techniques in imaging through turbid media. In fact, it is corroborated by evaluating the

Michelson contrast as a function of the spatial frequency. The Michelson contrast curves are shown in Figures 3.11(b) and 3.11(c) for the case of the SPI techniques, and in Figure 3.11(d) for the conventional imaging one, respectively.

Note also that the resolution of the conventional imaging system [Figure 3.11(d)] worsens quickly when the spatial filter diameter decreases further. The main reason is the low-pass filtering effect of the spatial frequencies, as was shown in Figure 3.6(c). In the case of the SPC that uses the PMT as a detector [Figure 3.11(c)], the image resolution is clearly better than that of the conventional system. It only deteriorates for very small pinholes because the SNR of the photocurrent provided by the PMT decreases for small diameters of the pinhole. However, in the case of the SPC using the CMOS image sensor [Figure 3.11(b)], the contrast of the images remains acceptable, even for very small pinholes, showing that SPI with Fourier filtering based on a digital camera filters scattering photons more efficiently. The reason is, again, the high sensitivity and SNR provided by the CMOS camera when many pixels are used together to record the signal. The advantage of performing the Fourier filtering digitally, after recording the whole set of projections, also influences, without doubt, the quality of the image. On the other hand, the acquisition speed is strongly limited by the frame rate of the camera, while the PMT permits higher frequency rates.

For the case of no pinhole, the image contrast is better with SPI techniques, because the sampling process in the SPC provides an inherent filtering effect. Highly scattered photons generate a uniform background pattern onto the object, instead of the well-defined WH pattern generated by the ballistic photons, which is eliminated when the positive and the complementary signals provided by the two patterns codifying each WH function are subtracted in the reconstruction process of the image.

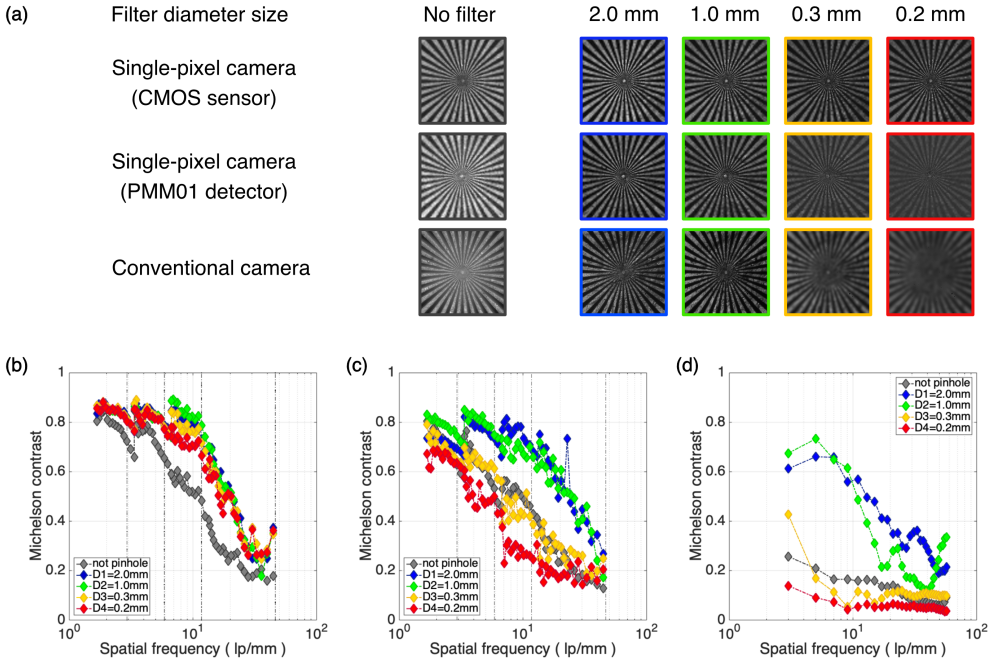

Figure 3.11: Experimental results with turbid medium. (a) Images recorded with different Fourier filtering conditions. In the first row, images obtained using the SPI technique and digital Fourier filtering. In the second one, images recovered using the SPC and Fourier filtering. In the last row, we show images obtained combining a conventional camera with Fourier filtering; (b), (c), and (d) are plots of the Michelson contrast curves versus the spatial frequency of images in (a).

3.5 Summary

In this chapter, we have developed a new imaging system combining SPI techniques with Fourier spatial filtering. We have compared the performance of our optical setup with that of a conventional imaging system based on Fourier filtering and using a CMOS camera as a detector. We have shown that, without scattering media, the single-pixel camera does not reduce the high frequency content of the object when a small pinhole is used as a low-pass filter at the detection side. Moreover, when the scattering media are introduced, the Fourier spatial filtering technique improves the contrast of the images in both cases, the single-pixel camera and the conventional one. We conclude that SPI fits better than conventional imaging in vision through turbid media by Fourier filtering. We note that this effect is present in many SPI configurations using a photosensor with a reduced size. Therefore, it may contribute to improve the image quality in other applications of SPI through scattering media.

Chapter 4

Infrared single-pixel imaging

The first experiment that demonstrated the existence of infrared (IR) radiation was done by Sir William Herschel (1738–1822 a.C.) 219 years ago. Herschel studied the sunlight spectrum measuring the temperature of each color and he found that the highest temperature was beyond the visible light, just below the red [91].

Since then, the use of IR radiation has opened an endless number of applications, including imaging through scattering media, in different areas pertaining to science and industry. In astronomy, for instance, IR radiation is used to study stellar structures such as galaxies and star clusters immersed in visible light disks or dust [92]. In medicine, fluorescence and thermal imaging in the IR spectral region, coupled with other techniques such as tomography or mammography, has attracted tremendous scientific interest due to the salient advantages of deep tissue penetration, fast imaging, clear visualization, and non-invasive diagnosis of diseases such as cancer or chronic pain [93–95]. In the industry, the applications range from the de-

sign of thermal cameras, which allow to analyze if the thermal isolation of a building is adequate or not, to the elaboration of complex security systems. IR radiation has also numerous applications in visual assistance through natural scattering environments, such as fog, dust, smoke, and rain of all modes of navigation of vehicular transport [96]. One of the most recent applications of IR imaging is the study of ancient buildings and the restoration of art paintings [97]. Figure 4.1 illustrates some of the aforementioned applications.

Figure 4.1: Comparison between visible and IR imaging in different circumstances: (a) stellar structure of the Andromeda galaxy; (b) human rescue in a smoke environment; (c) aircraft landing in a foggy environment; and (d) study and restoration of the painting *Madonna in Preghiera* (Extracted from [97–101]).

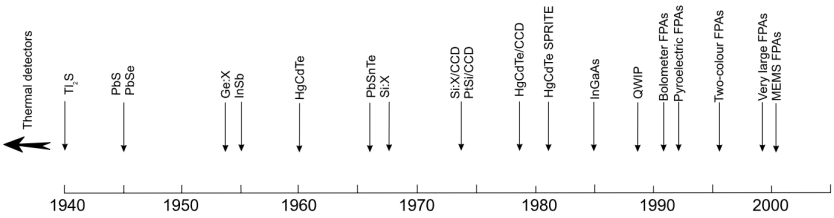

Figure 4.2: History of the development of IR detectors (Extracted from [102]).

On the other hand, many different kinds of IR detectors have been developed along the last century. [102, 103]. A timeline showing their evolution is illustrated in Figure 4.2. Because of this long history of research, a wide variety of detectors can be used nowadays, such as Germanium (Ge), Indium Gallium Arsenide (InGaAs), Indium Antimonide (InSb), and Mercury Cadmium Telluride (MCT or HgCdTe). Of these, InGaAs arrays detectors have proved to be the most practical for imaging applications due to their high quantum efficiency and low dark current at room temperature at an operating spectral range of (0.9–1.7 μm) [104]. However, despite all the technological advances made, to manufacture a camera with a large number of pixels, high quantum efficiency and low noise in the IR spectral region is still difficult. In this context, single-pixel cameras (SPCs) can be a practical and economical solution [105, 106].

In this chapter, several experiments for imaging through scattering media using an infrared SPC working by reflexion are described. In the subsequent section, first, a description of the experimental configuration of the IR SPC is made. Secondly, a study of the quality of the images based on the properties of the scattering media at a wavelength of 650 nm is shown. Afterward, a comparison of the performance of the SPC at the visible spectral region (650 nm) and NIR (800 nm) is shown.

4.1 Seeing through turbid water

In this section, an imaging system to obtain the image of an object hidden behind a turbid medium based on the SPI technique and a near-infrared (NIR) light source is described. In order to study a realistic case, the optical system is designed in a configuration by reflection. A schematic representation of the experimental setup is shown in Figure 4.3(a).

In our optical system, a DMD (DLP Discovery 7000, Texas Instrument) is illuminated uniformly with a collimated laser beam, which is generated by a supercontinuum laser source (FYLA SCT500 SN 0818-1) coupled to optical fiber, with a spectral range from 400 nm to 2400 nm. Microstructured light patterns corresponding to 2-D functions of the orthonormal WH basis with 64×64 pixels are coded on the DMD display in a chip area with 256×256 micromirrors with a micromirror pixel pitch of 13.7 μm. Each WH function is projected combining two patterns, one codifying the positive and the another the negative component of the function. A 4-f optical system formed by two achromatic lenses L1 and L2 is used to project the microstructured light patterns onto the object plane at a frame rate of 2 kHz. The focal distances of L1 and L2 are $f_1 = 100$ mm, and $f_2 = 200$ mm, respectively. A circular diaphragm is used at the back focal plane of lens L1 to filter unwanted diffracted orders produced by the periodic micromirror arrangement on the DMD. The light reflected on the object is collected by lens L2 and focused onto a Si variable-gain avalanche detector (APD410A/M, Thorlabs) located at the back focal point of L2. Additionally, to compare the performance of our SPC with that of a conventional one, a second 4-f imaging system formed by lenses L2 and L3 is carried out at the end of the previous setup as is shown in Figure 4.3(b). The focal distance of L3 is $f_3 = 100$ mm. In this case, a digital camera (UI-3370CP-NIR-GL,

IDS) with a CMOS image sensor of 1280 × 1024 pixels with a pitch of 5.5 μm is used as detector. In both experimental configurations, a positive 1951 USAF test target is used as object, and a water solution of milk on a glass cuvette in front of the object is used as turbid medium.

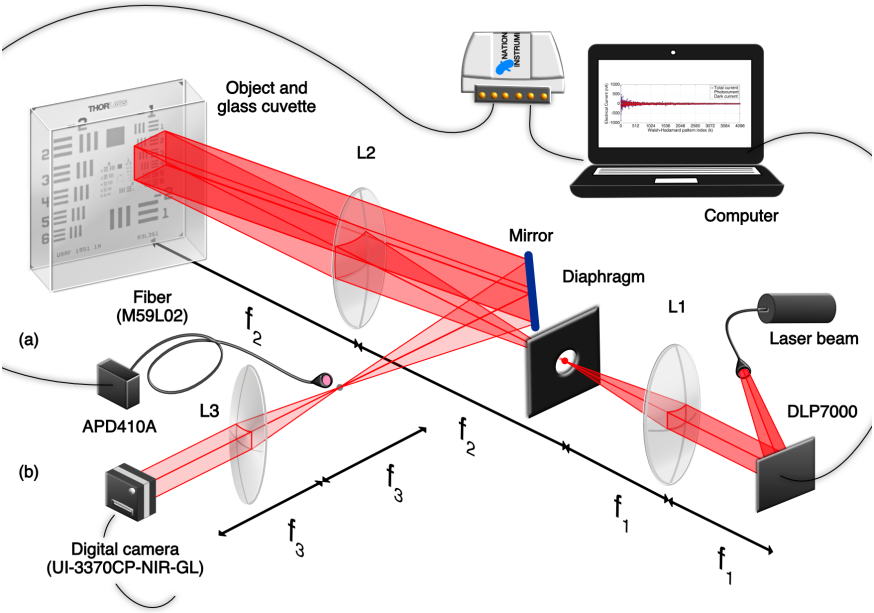

Figure 4.3: Experimental diagram of (a) the single-pixel camera, and (b) the conventional imaging setup working by reflection.

Milk is a very complex substance made up of spherical droplets of fat, called milk fat globules, suspended in a water solute [107]. Because of this, a strong scattering phenomenon occurs when light interacts with these particles. The white color of milk indicates that scattering is highly dominant in comparison to absorption throughout the visible wavelength range. For

our study, we selected a semi-skimmed milk. The fat globule size distribution was measured using a particle size analyzer based on laser diffraction (Masterizer 2000, Malven Instruments). It was estimated that the refractive index for milk fat is 1.460 at a wavelength of 633 nm, and 1.33 for water. The measurements were performed at room temperature. The resulting curve of the size distribution is shown in Figure 4.4(d). We note that the selected semi-skimmed milk is constituted mainly by two different sizes of milk fat globules, 0.15 and 0.6 microns. To corroborate this result, an image of the milk fat globules was taken using an optical microscope [see Figure 4.4(e)].

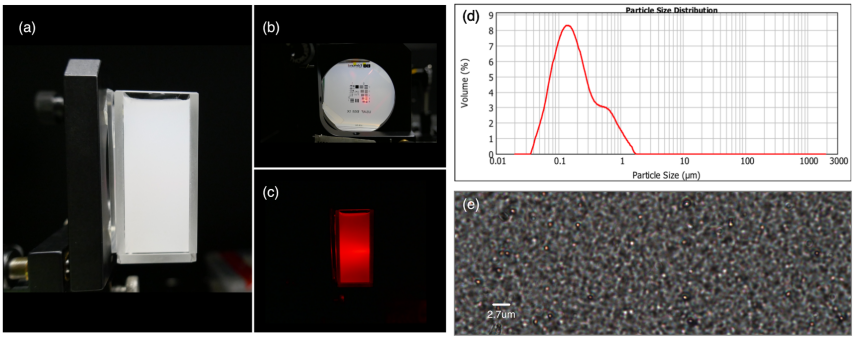

Figure 4.4: Object and turbid medium: (a) the water solution of milk into the glass cuvette; (b) the positive 1951 USAF test target placed hidden behind the glass cuvette in (a); (c) image of the cuvette showing the scattered light in the water solution of milk using a laser beam with a wavelength of 650 nm; (d) fat globule size distribution curve of the semi-skimmed milk obtained from the particle size analizer, and (e) microscope image of the milk fat globules. Scale bar= 2.7 μm.

To study experimentally the performance of the SPC as a function of the turbidity level in water, 13 water solutions of milk were prepared. In these solutions, we used 40 ml of distilled water as solvent and a variable of semi-skimmed milk as scattering agent. The range of milk proportion starts at

0.05 ml and ends at 0.6 ml in 0.05 ml steps. Distilled water is used as reference solution. A representative set of samples with different solutions is shown in Figure 4.5. In order to quantify the properties of the water solutions of milk, the optical depth (OD) and absorbance (A) parameters are measured.

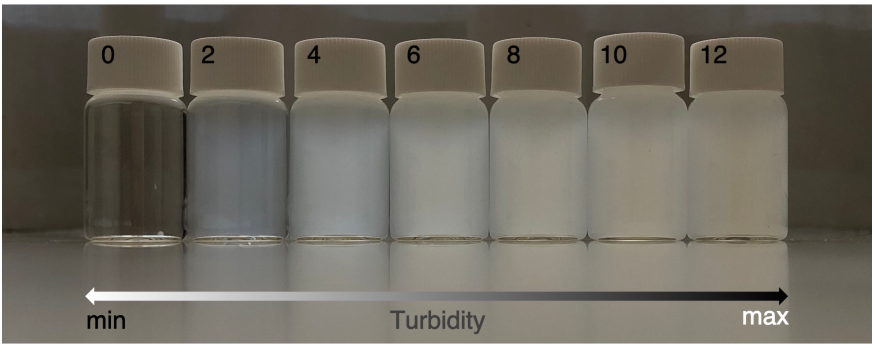

Figure 4.5: A representative set of samples with different solution using water and liquid milk. To prepare these solutions, we use 40 ml of distilled water and semi-skimmed milk. The milk range starts at 0.05 ml and ends at 0.6 ml in 0.05 steps. The turbidity increases from left to right as is shown by the lower bar.

In a reflection geometry, the intensity of single backscattered light I_R attenuates according to Beer's law as follows [78]:

$$I_R = I_0 e^{-2\mu_e \cdot d}, \tag{4.1}$$

where I_0 denotes the reference backscattered-light intensity, d is the sample thickness, μ_e is the extinction coefficient [cm^{-1}], and the factor of 2 in the exponent is due to the round-trip propagation. The optical depth, OD [dimensionless] is defined as:

$$\mathrm{OD} = 2d \cdot \mu_e = -\ln\left(\frac{I_R}{I_0}\right), \tag{4.2}$$

and the absorbance, A [dimensionless], is written as:

$$A = \frac{\mathrm{OD}}{\ln(10)}. \tag{4.3}$$

Parameters A and OD are frequently used to characterize turbid media. The first parameter, gives us a quick estimate of the amount of ballistic light that travels through the turbid medium, and the second one, the amount of scattering and/or absorption events occurred within the medium. For most turbid liquids, the resulting optical depth range is $2 \leq \mathrm{OD} \leq 9$, which corresponds to the intermediate scattering regime. On the other hand, if $\mathrm{OD} \leq 1$, the single backscattering regime is assumed, and if $\mathrm{OD} \geq 10$, the diffusive regimen is considered [108].

As is well known, the scattering properties of the medium depend strongly with the wavelength of the incident light. Many applications in biomedical optics research use wavelengths in the visible and near-infrared (NIR) spectral regions (from 400 to 1000 nm) [109]. In fact, visible light is very useful because it occupies the highest energy band that does not damage biological molecules [83]. In addition, some studies employ NIR radiation (800–1000 nm) to extract parameters related to tissue water and lipid concentrations on account of water and lipid have small absorption features near 970 and 930 nm, respectively. Moreover, to obtain more quantitative information about biological tissue constituents, it is also possible to extend the spectral region into the short-wave infrared (SWIR) radiation (∼1000 to 2000 nm). The main applications of SWIR radiation are assessment and monitoring of

burns, characterization of atherosclerotic plaque, and detection and monitoring of cancer [109]. In fact, it is obvious the enormous importance of the visible and IR radiation in the study of biological tissues composed mainly of water. In this context, we develop a study of imaging through turbid water, a water solution of milk, using two spectral windows centered in the visible and NIR spectral regions.

We quantified the optical depth and the absorbance of water solutions of milk using the optical system shown in Figure 4.3, and Equations 4.2 and 4.3. The process to measurement the ballistic backscattering light is described in Ref. [78]. To select the spectral windows, two narrow bandpass filters in the illumination system were used. One filter (P10-650-S 1B029, Corion) is centered at a wavelength of 650 nm with a bandwidth of 10 nm, for the visible region, and the second one (FB800-40 Thorlabs) is centered at a wavelength of 800 nm with a bandwidth of 40 nm, for the NIR region. The resulting data are shown in Table 4.1. The data obtained in the visible range are listed in the third and fourth columns, while those obtained in the NIR range are in the fifth and sixth columns. Note that, in both spectral regions, the values of OD and A increase as the amount of milk increases. However, as expected, the values in the NIR region are lower than in the visible one and increase slowly with the milk concentration.

We carried out several experiments of imaging through turbid media by using the optical arrangements shown in Figure 4.3 and the turbid water solutions described previously. The experimental results using light with a wavelength of 650 nm are shown in Figure 4.6. Images in the first row were obtained with the SPC, while those in the second row were recorded with the conventional one. Images in each column correspond to results obtained with different water solutions and turbidity: reference solution for the first column and solutions 2, 4, and 6 for the subsequent columns. Note

Table 4.1: Scattering parameters of water solutions of milk. The data obtained in the visible range are listed in the third and fourth columns, while those obtained in the NIR range are in the fifth and sixth columns.

No.	Milk[a] [ml]	OD	A	OD	A
1	0.05	1.89	0.82	0.61	0.27
2	0.10	2.59	1.12	1.01	0.44
3	0.15	3.76	1.64	1.36	0.59
4	0.20	4.23	1.84	1.88	0.82
5	0.25	5.15	2.30	2.39	1.04
6	0.30	5.84	2.54	3.49	1.52
7	0.35	–	–	3.96	1.72
8	0.40	–	–	4.47	1.94
9	0.45	–	–	4.88	2.30
10	0.50	–	–	5.57	2.42
11	0.55	–	–	6.08	2.64
12	0.60	–	–	6.77	2.94

[a] *Amount of semi-skimmed milk in 40 ml of water.*

that, in both optical systems, the influence of the scattering parameters of the medium is very noticeable on the quality of the recovered images. As expected, as the values of the optical depth (OD) and the absorbance (A) increase, the quality of the reconstructed images becomes worse. In highly scattering media, the number of ballistic photons that reach the detector is very low and, therefore the sensibility of the detector plays a very important role in the reconstruction process of the image. For instance, images corresponding to solution 6 are clearly noisier than those corresponding to the other solutions. In SPI techniques, the degradation of the SNR of the photocurrent provided by the detector, due to the loss of ballistic photons, causes a noisy background in the recorded images, while in the conventional

imaging systems, the main effect of the reduction of ballistic photons is the recording of dark noisy images. Note that in the case of the SPC, the gain of the APD was gradually increased, as the dispersion increased, until reaching its maximum value. On the other hand, for the conventional camera, it was the integration time that was increased up to the maximum value allowed by the camera while the camera gain remained constant. By adjusting the camera gain, a noisy image of the object can also recovered.

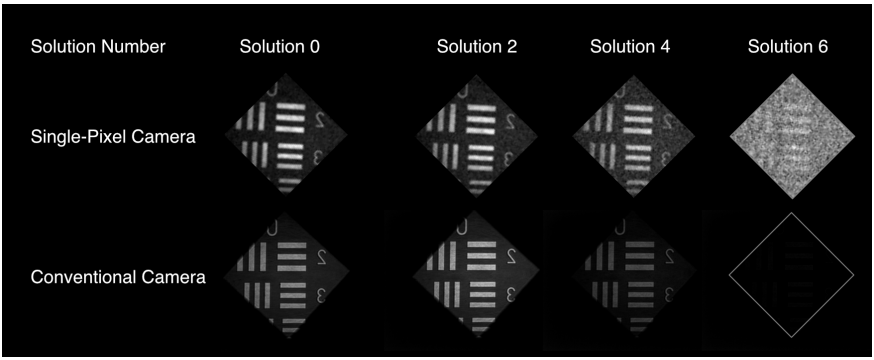

Figure 4.6: Experimental images recovered for different milk concentrations using light with a wavelength of 650 nm by employing (a) the SPC setup, and (b) the conventional one.

In order to do a comparative study of imaging through turbid media using SPI techniques, two different spectral windows were selected. We know that the diffuse component of the light scattering is strongly related to the wavelength of the incident light on the sample. In fact, we corroborated it by measuring the scattering parameters of the water solutions of milk at two different wavelengths, 650 nm, and 800 nm, as was shown in Table 4.1. Then, we selected the same spectral regions and carry out the imaging experiment using the SPC setup shown in Figure 4.3. The experimental results are shown in Figure 4.7. Images in the first row were obtained with visible

light, whereas those in the second row were recovered with NIR radiation. Images in each column correspond to results obtained using water solutions of milk with different scattering parameters: distilled water for the first column and solutions 3, 6, 9 and 12 for the subsequent columns. In both spectral regions, the quality of the images decreases as a function of the amount of milk. However, the quality of the images corresponding to NIR illumination is better than those corresponding to the visible one. These results suggest that it is possible to take images through scattering media using wavelengths beyond the visible light with SPI techniques, which opens the possibility to a wide range of applications in many fields such as health sciences, security, or surveillance industry.

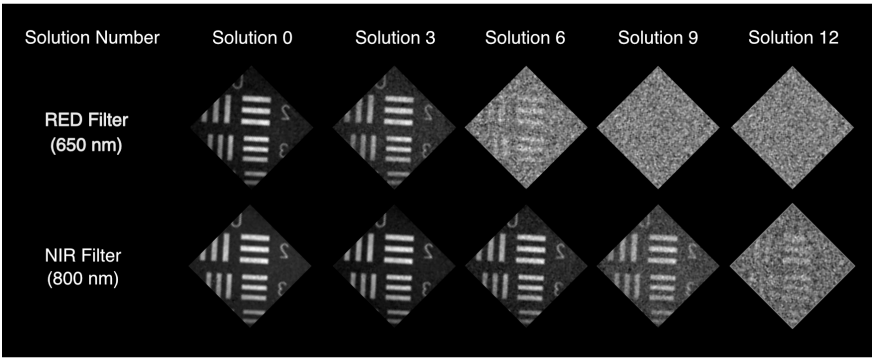

Figure 4.7: Experimental images of the positive 1951 USAF test target hidden behind different water solutions of milk into a glass cuvette. These images were obtained using the SPC working by reflection in two different spectral ranges.

4.2 Summary

In this chapter, we have studied experimentally the possibility of performing imaging through turbid water using a SPC with a double-pass configuration. In particular, two wavelengths corresponding to the visible (650 nm) and NIR (800 nm) spectral ranges were used. As a conclusion, it can be said that SPI techniques under NIR illumination are more efficient than those one working with visible light in imaging through scattering media. However, the quality of the images is not as good as expected in comparison with the conventional camera. Additionally, the studies carried out have also shown the importance of the optical properties of the scattering medium.

In general, the simplicity of the detection stage in SPI techniques is a relevant advantage over conventional imaging. In fact, it is easier and cheaper to build detectors with only one pixel, than with hundreds of these that work outside the spectral region of the visible. However, do not lose sight of the fact that in certain IR spectral windows the detectors may have more or less electronic noise.

These results suggest that it is possible to take images through scattering media using wavelengths beyond the visible light with SPI techniques, which opens a wide range of applications in many fields such as health sciences or security and surveillance industry.

Chapter 5

General conclusion and outlook

5.1 Conclusions

Imaging through scattering media is a challenging issue that has interested a large number of researchers for a long time, due to its relevance in biomedical imaging applications. Accordingly, many optical techniques have emerged to retrieve the information of objects hidden in highly scattering media, such as ultrafast time-gating imaging, polarization filtering, wavefront control methods based on measuring the transmission matrix or on adaptive techniques, and Fourier spatial filtering techniques. Besides, the use of radiation in spectral regions different to those that correspond to the visible range, in particular infrared radiation, has opened a wide range of applications in imaging through scattering media.

SPI techniques have proved to be a promising approach for imaging through scattering media. Some relevant advantages of SPI techniques come from

the use of very simple light sensors, that is, bucket detectors without pixelated structure. This fact has allowed to design cameras with high light efficiency, able to work in spectral regions out of the visible spectrum, and capable of performing multidimensional imaging with high flexibility. In the last decade, for instance, the SPC has been applied successfully in many different imaging areas. Among them, we can mention infrared imaging, terahertz imaging, ultrasonic imaging, 3D computational imaging, LIDAR, stereoscopic imaging, microscopy, holography, and ophthalmoscope imaging.

In this doctoral thesis, we have addressed the challenge of recovering the image of an object hidden behind scattering media. We have shown that SPI combined with the use of scattering filtering techniques and IR illumination allows designing very powerful and promising methods to tackle the problem. To achieve this goal, firstly, the nature of noise in SPCs has been thoroughly studied. In addition, new methods to reject the background noise generated by light scattering in imaging through turbid media have been developed.

In particular, we have developed a numerical model of SPCs based on photodiodes, which considers the characteristics of the incident light, as well as the photodiode specifications. The model takes into account many different kinds of electrical noise and infers the SNR of the SPC in three different circumstances: (1) when the optical power level of the light source changes; (2) at different optical wavelengths of the light source; and (3) when the photodiode temperature varies. The results of this model are compared with those obtained experimentally.

We have also shown a novel approach for imaging through scattering media that combines the SPI technique and the principles of Fourier spatial filtering. The performance of this approach has been compared with that of a conventional imaging system based on a CMOS camera. We have shown

that the Fourier filtering technique improves the spatial resolution of the images in both devices. Moreover, we have corroborated that SPI techniques behave better than conventional imaging in vision through turbid media by Fourier filtering. Additionally, we have proved that by using a CMOS camera as bucket detector, and performing Fourier filtering digitally, it is possible to improve the quality and efficiency of the images in comparison with those obtained with SPI methods based on PMTs.

Finally, several experiments for imaging through scattering media using an infrared SPC working by reflexion have been described. We have studied the quality of the images as a function of the scattering properties of turbid water samples and we have compared the performance of the SPC in two different spectral windows, visible and NIR.

5.2 Outlook

The different studies, algorithms, and techniques developed in this thesis could help to improve the performance of SPCs and to develop new relevant imaging applications in different fields. For instance, our numerical model for the SPC, conveniently updated to consider the influence of other sources of noise, could be used to optimize the behavior of SPI techniques under a large number of environmental conditions. The idea of using a digital image sensor as bucket detector in SPI might be further exploited to develop a smart SPC able to adapt to different light levels automatically. Furthermore, all these improvements could be utilized to design an IR camera based on single-pixel imaging techniques, well adapted to record high-quality images in turbid environments such as fog, smoke and turbid water. In all cases, it will be necessary to improve the image acquisition rate by using faster

SLM devices or new CS methods. Of course, our main motivation, and one of the purposes of all this research work, is to develop new optical imaging methods for biomedical applications with better performance in terms of resolution and penetration depth.

Bibliography

[1] A. Wax and V. Backman, *Biomedical Applications of Light Scattering* (McGraw Hill Professional, 2009).

[2] V. Ntziachristos, "Going deeper than microscopy: the optical imaging frontier in biology," Nat. Meth. **7**, 8603–8614 (2010).

[3] L. Wang, P. P. Ho, C. Liu, G. Zhang, and R. R. Alfano, "Ballistic 2-D imaging through scattering walls using an ultrafast optical Kerr gate," Science **253**, 769–771 (1991).

[4] M. Xu, R. R. Alfano, "Random walk of polarized light in turbid media," Phys. Rev. Lett. **95**, 213901 (2005).

[5] N. K. Soni, R. V. Vinu, and R. K. Singh, "Polarization modulation for imaging behind the scattering medium," Opt. Lett. **41**, 906–909 (2016).

[6] H. B. de Aguiar, S. Gigan, and Sophie Brasselet, "Polarization recovery through scattering media," Sci. Adv. **3**, e1600743 (2017).

[7] S. M. Popoff, G. Lerosey, R. Carminati, M. Fink, A. C. Boccara, and S. Gigan,"Measuring the transmission matrix in optics: an approach

to the study and control of light propagation in disordered media," Phys. Rev. Lett. **104**, 100601 (2010).

[8] J. Bertolotti, E. G. van Putten, C. Blum, A. Lagendijk, W. L. Vos, and A. P. Mosk, "Non-invasive imaging through opaque scattering layers," Nature **491**, 232–234 (2012).

[9] Q. Z. Wang, X. Liang, L. Wang, P. P. Ho, and R. R. Alfano, "Fourier spatial filter acts as a temporal gate for light propagating through a turbid medium," Opt. Lett. **20**, 1498–1500 (1995).

[10] E. Berrocal, S. G. Pettersson, and E. Kristensson, "High-contrast imaging through scattering media using structured illumination and Fourier filtering," Opt. Lett. **41**, 5612–5615 (2016).

[11] A. D. Rodríguez, P. Clemente, E. Irles, E. Tajahuerce, and J. Lancis, "Resolution analysis in computational imaging with patterned illumination and bucket detection," Opt. Lett. **39**, 3888–3891 (2014).

[12] E. Tajahuerce, V. Durán, P. Clemente, E. Irles, F. Soldevila, P. Andrés, and J. Lancis, "Image transmission through dynamic scattering media by single-pixel photodetection," Opt. Express **22**, 16945–16955 (2014).

[13] Z. A. Steelman, D. S. Ho, K. K. Chu, and A. Wax, "Light-scattering methods for tissue diagnosis," Optica **6**, 479–489 (2019).

[14] M. F. Duarte, M. A. Davenport, D. Takbar, J. N. Laska, T. Sun, K. F. Kelly, and R. G. Baraniuk, "Single-Pixel Imaging via Compressive Sampling," IEEE Signal Process. Mag. **25**, 83–91 (2008).

[15] J. H. Shapiro, "Computational ghost imaging," Phys. Rev. A **78**, 061802 (2008).

[16] Y. Bromberg, O. Katz, and Y. Silberberg, "Ghost imaging with a single detector," Phys. Rev. A **79**, 053840 (2009)

[17] B. I. Erkmen and J. H. Shapiro, "Ghost imaging: from quantum to classical to computational," Adv. Opt. Photon. **2**, 405–450 (2010).

[18] M. G. Padgett and R. W. Boyd, "An introduction to ghost imaging: quantum and classical," Phil. Trans. R. Soc. A. **375**, 20160233 (2017).

[19] P. Sen, et al., "Dual photography," ACM Trans. Graph. **24**, 745–755 (2005).

[20] V. Studer, J. Bobin, M. Chahid, H. S. Mousavi, E. Candes, and M. Dahan, "Compressive fluorescence microscopy for biological and hyperspectral imaging," Proc. Natl. Acad. Sci. USA **109**, E1679–E1687 (2012).

[21] G. A. Howland, D. J. Lum, M. R. Ware, and J. C. Howell,"Photon counting compressive depth mapping," Opt. Express **21**, 23822–23837 (2013).

[22] F. Soldevila, E. Irles, V. Durán, P. Clemente, M. Fernández-Alonso, E. Tajahuerce, and J. Lancis, "Single-pixel polarimetric imaging spectrometer by compressive sensing," Appl. Phys. B **113**, 551–559 (2013).

[23] V. Durán, P. Clemente, M. Fernández-Alonso, E. Tajahuerce, and J. Lancis, "Single-pixel polarimetric imaging," Opt. Lett. **37**, 824–826 (2012).

[24] V. Durán, F. Soldevila, E. Irles, P. Clemente, E. Tajahuerce, P. Andrés, and J. Lancis, "Compressive imaging in scattering media," Opt. Express **23**, 14424–14433 (2015).

[25] Y. K. Xu, W. T. Liu, E. F. Zhang, Q. Li, H. Y. Dai, and P. X. Chen, "Is ghost imaging intrinsically more powerful against scattering?," Opt. Express **23**, 32993–33000 (2015).

[26] M. J. E. Golay, "Multi-Slit Spectrometry*," J. Opt. Soc. Am. **39**, 437–444 (1949).

[27] J. A. Decker, "Hadamard–Transform Image Scanning," Appl. Opt. **9**, 1392–1395 (1970).

[28] M. B. Wakin, J. N. Laska, M. F. Duarte, D. Baron, S. Sarvotham, D. Takhar, K. F. Kelly, and R. G. Baraniuk, "An architecture for compressive imaging," 2006 International Conference on Image Processing IEEE, 1273–1276 (2006).

[29] H. Chen, N. Xi, B. Song, L. Chen, J. Zhao, K. W. C. Lai, and R. Yang, "Infrared camera using a single nano-photodetector," IEEE Sens. J. **13**, 949–958 (2013).

[30] G. M. Gibson, B. Sun, M. P. Edgar, D. B. Phillips, N. Hempler, G. T. Maker, G. P. A. Malcolm, and M. J. Padgett, "Real-time imaging of methane gas leaks using a single-pixel camera," Opt. Express **25**, 2998–3005 (2017).

[31] R. I. Stantchev, B. Sun, S. M. Hornett, P. A. Hobson, G. M. Gibson, M. J. Padgett, and E. Hendry, "Noninvasive, near-field terahertz imaging of hidden objects using a single-pixel detector," Sci. Adv. **2**, e1600190 (2016).

[32] N. Huynh, E. Zhang, M. Betcke, S. Arridge, P. Beard, and B. Cox, "Single-pixel optical camera for video rate ultrasonic imaging," Optica **3**, 26–29 (2016).

[33] B. Sun, M. P. Edgar, R. Bowman, L. E. Vittert, S. Welsh, A. Bowman, and M. J. Padgett, "3D computational imaging with single-pixel detectors," Science **340**, 844–847 (2013).

[34] J. Hunt, T. Driscoll, A. Mrozack, G. Lipworth, M. Reynolds, D. Brady, and D. R. Smith, "Metamaterial apertures for computational imaging," Science **339**, 310–313 (2013).

[35] J. Shin, B.T. Bosworth, and M. A. Foster, "Single-pixel imaging using compressed sensing and wavelength-dependent scattering," Opt. Lett. **41**, 886–889 (2016).

[36] Y. Jauregui-Sánchez, P. Clemente, J. Lancis, and E. Tajahuerce, "Single-pixel imaging with Fourier filtering: application to vision through scattering media," Opt. Lett. **44**, 679–682 (2019)

[37] A. Kirmani, D. Venkatraman, D. Shin, A. Colaço, F. N. C. Wong, J. H. Shapiro, V. K. Goyal, "First-Photon Imaging," Science **343**, 58–61 (2014).

[38] M. J. Sun, M. P. Edgar, G. M. Gibson, B. Sun, N. Radwell, R. Lamb, and M. J. Padgett, "Single-pixel three-dimensional imaging with time-based depth resolution," Nat. Commun. **7**, 12010 (2016).

[39] E. Salvador-Balaguer, P. Clemente, E. Tajahuerce, F. Pla, and J. Lancis, "Full-color stereoscopic imaging with a single-pixel photodetector," J. Display Technol. **12**, 417–422 (2016).

[40] N. Radwell, K. J. Mitchell, G. M. Gibson, M. P. Edgar, R. Bowman, and M. J. Padgett, "Single-pixel infrared and visible microscope," Optica **1**, 285–289 (2014.)

[41] A. D. Rodríguez, P. Clemente, E. Tajahuerce, and J. Lancis, "Dual-mode optical microscope based on single-pixel imaging," Opt. Lasers Eng. **82**, 87–94 (2016).

[42] D. J. Brady, K. Choi, D. L. Marks, R. Horisaki, and S. Lim, "Compressive Holography," Opt. Express **17**, 13040–13049 (2009).

[43] Ll. Martínez-León, P. Clemente, Y. Mori, V. Climent, J. Lancis, and E. Tajahuerce, "Single-pixel digital holography with phase-encoded illumination," Opt. Express **25**, 4975–4984 (2017).

[44] B. Lochocki, A. Gambín, S. Manzanera, E. Irles, E. Tajahuerce, J. Lancis, and P. Artal, "Single pixel camera ophthalmoscope," Optica **3**, 1056–1059 (2016).

[45] N. Savage, "Digital spatial light modulators," Nat. Photonics. **3**, 170–172 (2009).

[46] Y. X. Ren, R. D. Lu, and L. Gong, "Tailoring light with a digital micromirror device," Ann. Phys. **527**, 447–470 (2015).

[47] DLP Discovery 4100 Development Kit, Texas Instruments, 2018 [Online]. Available from: http://www.ti.com/tool/DLPD4X00KIT# [Accessed: 2018-06-11].

[48] R. G. Baraniuk, T. Goldstein, A. C. Sankaranarayanan, C. Studer, A. Veeraraghavan, and M. B. Wakin, "Compressive video sensing: Algorithms, architectures, and applications," IEEE Signal Process. Mag. **34**, 52–66 (2017).

[49] P. Clemente, *Sistemes formadors dÍmatges multidimensionals amb detecció integrada* [thesis], Universitat Jaume I, Spain (2015).

[50] Texas Instruments DLP digital micromirror device [Online]. Available from: https://commons.wikimedia.org/wiki/File:Texas_Instruments_DLP_digital_micromirror_device_-_(1).jpg [Accessed: 2019-06-06].

[51] Micromirror arragment on a DLP chip [Online]. Available from: https://www.viewsonic.com/library/entertainment/what-look-for-dlp-projector [Accessed: 2019-06-06].

[52] E. J. Candès and M. B. Walkin, "An introduction to compressive sampling," IEEE Signal Process. Mag. **25**, 21–30 (2008).

[53] R. M. Willett, R. F. Marcia, and J. M. Nichols, "Compressed sensing for practical optical imaging systems: a tutorial," Opt. Eng. **50**, 072601 (2011).

[54] F. Soldevila, E. Salvador-Balaguer, P. Clemente, E. Tajahuerce, and J. Lancis, "High-resolution adaptive imaging with a single photodiode," Sci. Rep. **5**, 14300 (2015).

[55] D. B. Phillips, M. J. Sun, J. M. Taylor, M. P. Edgar, S. M. Barnett, G. M. Gibson, and M. J. Padgett, "Adaptive foveated single-pixel imaging with dynamic supersampling," Sci. Adv. **3**, e1601782 (2017).

[56] A. Pastuszczak, B. Szczygieł, M. Mikołajczyk, and R. Kotyński, "Efficient adaptation of complex-valued noiselet sensing matrices for compressed single-pixel imaging," Appl. Opt. **55**, 5141–5148 (2016).

[57] F. Rousset, N. Ducros, A. Farina, G. Valentini, C. D' Andrea, and F. Peyrin, "Adaptive basis scan by wavelet prediction for single-pixel imaging," IEEE Transactions on Computational Imaging **4**, 284–294 (2018).

[58] Z. Zhang, X. Wang, G. Zheng, and J. Zhong, "Hadamard single-pixel imaging versus Fourier single-pixel imaging," Opt. Express **25**, 19619–19639 (2017).

[59] A. K. Jain, *Fundamentals of digital image processing* (Prentice Hall, 1989); ISBN: 0-13-336165-9.

[60] W. K. Pratt, J. Kane, and H. C. Andrews, "Hadamard transform image coding," Proc. IEEE **57**, 58–68 (1969).

[61] W. K. Pratt, *Digital Image Processing* (John Wiley & Sons Inc., 2007); ISBN: 978–0471767770.

[62] R. E. A. C. Paley, "On orthogonal matrices," J. Math. Phys. **12**, 311–320 (1933).

[63] S. M. Sze and K. K. Ng, *Physics of Semiconductor Devices* (John Wiley & Sons Inc., 2007); ISBN-13: 978-0471143239.

[64] G. P. Agrawal, *Fiber-optic communication systems* (John Wiley & Sons Inc., 2010); ISBN-13: 978-0470505113.

[65] T. Pearsall, M. Piskorski, A. Brochet, and J. Chevrier, "A $Ga_{0.47}In_{0.53}As$/InP heterophotodiode with reduced dark current," IEEE J. Quantum Electron. **17**, 255–259 (1981).

[66] K. Ohnaka, M. Kubo, J. Shibata, "A Low Dark Current InGaAs/InP p-i-n Photodiode with Covered Mesa Structure," IEEE Trans. Electron Devices **34**, 199–204 (1987).

[67] B. Jacob, B. Witzigmann, M. Klemenc, and C. Petit, "A TCAD methodology for high-speed photodetectors," Solid-State Electron. **49**, 1002–1008 (2005).

[68] Y. P. Varshni, "Temperature dependence of the energy gap in semiconductors," Physica **34** 149–154 (1967).

[69] Sajal Paul, J. B. Roy, and P. K. Basu, "Empirical expressions for the alloy composition and temperature dependence of the band gap and intrinsic carrier density in $Ga_xIn_{1-x}As$," J. Appl. Phys. **69**, 827–830 (1991).

[70] M. Konnik, J. Welsh, "High-level numerical simulations of noise in CCD and CMOS photosensors: Review and tutorial", arXiv preprint **arXiv:1412.4031** (2014).

[71] I. Vurgaftman, J.R. Meyer and L.R. Ram-Mohan, "Band parameters for III-V compound semiconductors and their alloys," J. Appl. Phys. **89**, 5815–5875 (2001).

[72] W. R. Bennett, "Sources and properties of electrical noise," Electrical Engineering **73**, 1001–1006 (1954).

[73] R. C. Gonzalez and R. E. Woods, *Digital Image Processing* (Prentice Hall, 2008); ISBN-13: 978–0131687288.

[74] Y. Jauregui-Sánchez, P. Clemente, P. Latorre-Carmona, E. Tajahuerce, and J. Lancis, "Signal-to-noise ratio of single-pixel cameras based on photodiodes," Appl. Opt. **57**, B67–B73 (2018).

[75] Si Biased Detector DET36A Thorlabs, Inc., 2018 [Online]. Available from: https://www.thorlabs.com/thorproduct.cfm?partnumber=DET36A [Accessed: 2018-06-21].

[76] InGaAs Biased Detector DET10C Thorlabs, Inc., 2018 [Online]. Available from: https://www.thorlabs.com/thorproduct.cfm?partnumber=DET10C [Accessed: 2018-06-21].

[77] Y. Jauregui-Sánchez, P. Clemente, P. Latorre-Carmona, J. Lancis, and E. Tajahuerce, *Single-Pixel Imaging using Photodiodes* (IntechOpen, 2018). Available from: https://www.intechopen.com/online-first/single-pixel-imaging-using-photodiodes [Accessed: 2018-12-08].

[78] L. V. Wang, and H. I. Wu, *Biomedical Optics: principles and imaging* (John Wiley & Sons Inc., 2007); ISBN: 978–0471743040.

[79] S. L. Jacques, B. W. Pogue, "Tutorial on diffuse light transport," J. Biomed. Opt. **13**, 041302 (2008).

[80] S. Rotter, and S. Gigan, "Light fields in complex media: mesoscopic scattering meets wave control," Rev. Mod. Phys. **89**, 015005 (2017).

[81] V. Tuchin, *Tissue optics: Light scattering methods and instruments for medical diagnostics* (SPIE Press, 2015); ISBN: 978–1628415162.

[82] C. Dunsby, and P. M. W. French,"Techniques for depth-resolved imaging through turbid media including coherence-gated imaging," J. Phys. D. Appl. Phys. **36**, R207–R227 (2003).

[83] S. Kang, S. Jeong, W. Choi, H. Ko, T. D. Yang, J. H. Joo, Jae-S. Lee, Yong-S. Lim, Q-H. Park and W. Choi, "Imaging deep within a scattering medium using collective accumulation of single-scattered waves," Nat. Photonics **9**, 253–258 (2015).

[84] D. A. Boas, D. H. Brooks, E. L. Miller, C. A. DiMarzio, M. Kilmer, R. J. Gaudette, and Q. Zhang, "Imaging the body with diffuse optical tomography," IEEE Signal Proc. Magazine **18**, 57–75 (2001).

[85] S. Gigan, "Optical microscopy aims deep," Nat. Photonics **11**, 14-16 (2017).

[86] A. P. Mosk, A. Lagendijk, G. Lerosey, and M. Fink, "Controlling waves in space and time for imaging and focusing in complex media," Nat. Photonics **6**, 283–292 (2012).

[87] D. Huang, E. A. Swanson, C. P. Lin, J. S. Schuman, W. G. Stinson, W. Chang, M. R. Hee, T. Flotte, K. Gregory, C. A. Puliafito, and J. G. Fujimoto, "Optical Coherence Tomograpghy," Science **254**, 1178–1181 (1991).

[88] A. Badon, D. Li, G. Lerosey, A. C. Boccara, M. Fink, and Alexandre Aubry, "Smart optical coherence tomography for ultra-deep imaging through highly scattering media," Sci. Adv. **2**, e1600370 (2016).

[89] S. C. Park, M. K. Park, and M. G. Kang, "Super-resolution image reconstruction: a technical overview," IEEE Signal Process. Mag. **20**, 21–36 (2003).

[90] Y. Jauregui-Sánchez, P. Clemente, J. Lancis, and E. Tajahuerce, "Imaging through scattering media by Fourier filtering and single-pixel detection", Proc. SPIE 10502, Adaptive Optics and Wavefront Control for Biological Systems IV, 105020W (2018).

[91] W. Herschel, "Experiments on the refrangibility of the invisible rays of the Sun," Phil. Trans. Roy. Soc. London **90**, 284–292 (1800).

[92] J. A. Cardelli, G. C. Clayton, and J. S. Mathis, "The relationship between infrared, optical, and ultraviolet extinction," Astrophysical Journal **345**, 245–256 (1989).

[93] E. F. J. Ring, and K. Ammer, "Infrared thermal imaging in medicine," Physiol. Meas. **33**, R33–R46 (2012).

[94] G. Hong, A. L. Antaris, and H. Dai, "Near-infrared fluorophores for biomedical imaging," Nat. Biomed. Eng. **1**, 0010 (2017).

[95] J. Qi, C. Sun, A. Zebibula, H. Zhang, R. T. K. Kwok, X. Zhao, W. Xi, J. W. Y. Lam, J. Qian and B. Z. Tang, "Real-Time and High-Resolution Bioimaging with Bright Aggregation-Induced Emission Dots in Short-Wave Infrared Region," Adv. Mater. **30**, 1706856 (2018).

[96] J. Fade, S. Panigrahi, A. Carré, L. Frein, C. Hamel, F. Bretenaker, H. Ramachandran, and M. Alouini, "Long-range polarimetric imaging through fog," Appl. Opt. **53**, 3854–3865 (2014).

[97] J. Dong, A. Locquet, M. Melis, and D. S. Citrin, "Global mapping of stratigraphy of an old-master painting using sparsity-based terahertz reflectometry," Sci. Rep. **7**,15098 (2017).

[98] Visible image of Andromeda galaxy structure [Online]. Available from: https://apod.nasa.gov/apod/image/1306/m31_comolli_2193.jpg [Accessed: 2019-05-04].

[99] Infrared image of Andromeda galaxy structure [Online]. Available from: https://es.m.wikipedia.org/wiki/Archivo:Andromeda_galaxy_Ssc2005-20a1.jpg [Accessed: 2019-05-04].

[100] Human rescue in a dense smoke environment [Online]. Available from: http://coolcosmos.ipac.caltech.edu/page/firefighting [Accessed: 2019-05-04].

[101] Aircraft landing in a foggy environment [Online]. Available from: https://www.globalweatherclimatecenter.com/aviation-topics# [Accessed: 2019-05-04].

[102] A. Rogalski, "Infrared detectors: an overview," Infrared Phys. Technol. **43**, 187–210 (2002).

[103] A. Rogalski, "History of infrared detectors," Opto-Electron. Rev. **20**, 279–308 (2012).

[104] M. P. Hansen, and D. S. Malchow, "Overview of SWIR detectors, cameras, and applications," Proc. SPIE Thermosense XXX **6939**, 69390l (2008).

[105] R. S. Aspden, N. R. Gemmell, P. A. Morris, D. S. Tasca, L. Mertens, M. G. Tanner, R. A. Kirkwood, A. Ruggeri, A. Tosi, R. W. Boyd, G. S. Buller, R. H. Hadfield, and M. J. Padgett, "Photon-sparse microscopy: visible light imaging using infrared illumination," Optica **2**, 1049–1052 (2015).

[106] G. M. Gibson, B. Sun, M. P. Edgar, D. B. Phillips, N. Hempler, G. T. Maker, G. P. A. Malcolm, and M. J. Padgett, "Real-time imaging of methane gas leaks using a single-pixel camera," Opt. Express **25**, 2998–3005 (2017).

[107] O. Ménard, S. Ahmad, F. Rousseau, V. Briard-Bion, F. Gaucheron, and C. Lopez, "Buffalo vs. Cow milk fat globules: size distribution, zeta-potential, compositions in total fatty acids and in polar lipids from the milk fat globule membrane," Food Chemistry **120**, 544–551 (2010).

[108] E. Berrocal, D. L. Sedarsky, M. E. Paciaroni, I. V. Meglinski, and M. A. Linne, "Laser light scattering in turbid media Part I: Experimental and simulated results for the spatial intensity distribution," Opt. Express **15**, 10649–10665 (2007).

[109] R. H. Wilson, K. P. Nadeau, F. B. Jaworski, B. J. Tromberg, and A. J. Durkin, "Review of short-wave infrared spectroscopy and imaging methods for biological tissue characterization," J. Biomed. Opt. **20**, 030901 (2015).

List of Figures

List of Tables